Chemical Engineering Research and Design 205 (2024) 695–712

Contents lists available at ScienceDirect

Chemical Engineering Research and Design

journal homepage: www.elsevier.com/locate/cherd

Experimental analysis of lifelines in a 15,000 L bioreactor by means of Lagrangian Sensor Particles

Sebastian Hofmann [a,*], Lukas Buntkiel [b], Ryan Rautenbach [a], Lena Gaugler [c], Yifan Ma [b], Ingrid Haase [a], Jürgen Fitschen [d], Thomas Wucherpfennig [d], Sebastian Felix Reinecke [b], Marko Hoffmann [a], Ralf Takors [c], Uwe Hampel [b,e], Michael Schlüter [a]

[a] Institute of Multiphase Flows, Hamburg University of Technology, Eißendorfer Strasse 38, 21073 Hamburg, Germany
[b] Helmholtz-Zentrum Dresden-Rossendorf, Bautzner Landstraße 400, 01328 Dresden, Germany
[c] Institute of Biochemical Engineering, University of Stuttgart, Allmandring 31, 70569 Stuttgart, Germany
[d] Late Stage USP Development, Bioprocess Development Biologicals, Boehringer Ingelheim Pharma GmbH & Co. KG, Germany
[e] Chair of Imaging Techniques in Energy and Process Engineering, TUD Dresden University of Technology, 01062 Dresden, Germany

ARTICLE INFO

Dataset link: Gitlab project, DaRUS repository

Keywords:
Lagrangian Sensor Particles
Circulation time distribution
Residence time distribution
Lagrangian regime analysis
Elephant Ear impellers
Industrial scale

ABSTRACT

This study employs Lagrangian Sensor Particles (LSPs) with a diameter of 40 mm equipped with a pressure sensor to investigate cell lifelines in a 15,000 L stirred tank reactor (STR) with three Elephant Ear impellers. The Stokes number of the LSPs is approx. 0.004 on a macro-scale. The vertical probability of presence, axial velocity profiles, circulation time distributions, and residence time distributions are quantified to analyze single-phase mixing heterogeneities, detect hydrodynamic compartments and conduct a Lagrangian regime analysis. Results reveal a similarly distributed probability of presence in the vertical reactor center but emphasize the LSP's sensitivity to fluctuating densities. Axial velocity distributions illustrate characteristic impeller-induced flow patterns, and circulation time distributions identify three compartments with comparatively shorter times in the axial center. Residence time distributions exhibit a similar compartmentalized profile. Moreover, the study estimates a potential oxygen deprivation zone for CHO cells in the upper compartment and demonstrates the LSP's efficacy in characterizing impeller systems. Contrary to literature, the ratio of examined global mixing times to circulation times is 1.0, highlighting macro-scale mixing. The research underscores that LSPs offer crucial insights into industrial-scale STRs, specifically for determining hydrodynamic compartments without having optical access.

1. Introduction

In recent decades, the field of biotechnology has experienced substantial progress in genetic engineering, mammalian cell culture and genomics and proteomics, leading to the development of advanced biotechnological processes. For instance, after the development of artificial microbial consortia for biotechnological production processes on laboratory scale (Mittermeier et al., 2022; Herzog et al., 2023; Kratzl et al., 2023), large-scale bioreactors with volumes up to 30 m^3, and more can be utilized (Larsson et al., 1996; Vrábel et al., 2000). To do so, process monitoring and process control are critical elements to ensure reproducibility, maintain high-quality standards and enhance efficiency and productivity. However, when scaling up bioprocesses, there is often a reduction in productivity (Nadal-Rey et al., 2021b). This may be attributed to the emergence of population heterogeneities within the culture (Nadal-Rey et al., 2021b; Hoang et al., 2022; Rugbjerg and Sommer, 2019; Takors, 2012; Enfors et al., 2001; Heins et al., 2015), stemming from non-ideal dynamic conditions. Such temporal and spatial gradients originate from mixing heterogeneities within the bioreactor in form of compartments (Rosseburg et al., 2018; Kuschel and Takors, 2020; Nadal-Rey et al., 2021a; Weiland et al., 2023), which might furthermore emerge from an overestimated sensitivity of the cells to shear stress (Nienow et al., 2013), and therefore deteriorate key performance criteria such as titer, rates and yield (George et al., 1998; Lara et al., 2006). Similar scenarios and gradients can be investigated on microfluidic chips (Ho et al., 2019, 2022) or mimicked in scale-down reactors on laboratory scale by using e.g. flow-inhibiting elements or separate cultivation units. This enables to investigate cell-bioreactor interactions more thoroughly, as was reviewed by Neubauer and Junne (Neubauer and Junne, 2010), and more recently, by Nadal-Rey et al. (2021b). On that account, large-scale data regarding

* Corresponding author.
E-mail addresses: sebastian.hofmann@tuhh.de (S. Hofmann), l.buntkiel@hzdr.de (L. Buntkiel).

https://doi.org/10.1016/j.cherd.2024.04.015
Received 30 November 2023; Received in revised form 19 March 2024; Accepted 10 April 2024
Available online 15 April 2024

Nomenclature

Arabic symbols

A	Area/m^2
Ar	Archimedes number/–
b	Baffle width/m
C	Impeller off-bottom clearance/m
c	Concentration/ $g\,L^{-1}$
c_D	Drag coefficient/–
d_{imp}	Impeller diameter/m
d_{LSP}	LSP diameter/mm
d_p	Particle diameter/mm
d_{STR}	Reactor diameter/m
f	Sampling frequency/Hz
g	Gravitational acceleration/$m\,s^{-2}$
H	Reactor filling height/m
h	Impeller spacing/m
K	Henry coefficient/$Pa\,m^3\,mol^{-1}$
k_{to}	Turn-over constant/–
L	Characteristic length scale/m
L_E	Taylor scale/m
M	Total number of counts in dataset/–
m_{LSP}	LSP mass/g
n	Impeller frequency/rpm
$N_{Q,c}$	Circulation Flow number/–
$N_{Q,e}$	Exchange Flow number/–
$N_{Q,p}$	Pumping number/–
$N_{Q,r}$	Residence Flow number/–
N_j	Number of counts in bin j/–
P	Power input/W
p	Pressure/Pa
$P\,V^{-1}$	Global power per volume input/ $W\,m^{-3}$
p_0	Ambient pressure/Pa
Po	Power number/–
r	Radial distance/m
Re_{STR}	Global Reynolds number/–
Re_p	Particle Reynolds number/–
St	Stokes number/–
T	Temperature/ °C
t	Time/s
t_{circ}	Circulation time/s
u	Velocity of the fluid/ $m\,s^{-1}$
u_0	Root mean square of fluid velocity/ $m\,s^{-1}$
u_{tip}	Impeller tip speed/ $m\,s^{-1}$
V	Reactor working volume/ m^3
v	Velocity of the LSP/ $m\,s^{-1}$
v_z	Axial velocity/ $m\,s^{-1}$
z	Specific height in reactor/m

Greek symbols

Δ	Uncertainty
δ	Difference
η	Dynamic viscosity/Pa s
λ_K	Kolmogorov length scale/m
$\lambda_{K,\Phi}$	Min. Kolmogorov length scale/m
ν	Kinematic viscosity/$m^2\,s^{-1}$
Φ	Local energy dissipation ratio/–
ϕ	Sphericity/–
ρ	Density/ $kg\,m^{-3}$
ρ_f	Fluid density/ $kg\,m^{-3}$
ρ_p	LSP density/ $kg\,m^{-3}$
τ	Residence time/s
τ_f	Characteristic time of the flow field/s
τ_p	Particle response time/s
ε_T	Energy dissipation rate/$W\,kg^{-1}$
ξ^*	Mass concentration/$kg\,m^{-3}$

Abbreviations

CHO	Chinese hamster ovary
CTD	Circulation time distribution
DW	Deionized water
EE	Elephant Ear
HCl	Hydrochloric acid
HZDR	Helmholtz-Zentrum Dresden-Rossendorf
IP	Injection point
IS	Isotonic solution
LSP	Lagrangian Sensor Particle
NaCl	Sodium chloride
NaOH	Sodium hydroxide
PBT-4	4-bladed pitched blade turbine
PBT-6	6-bladed pitched blade turbine
rms	Root mean square
RT-6	6-bladed Rushton turbine
RTD	Residence time distribution
STR	Stirred tank reactor

circulation times (Reinecke et al., 2012), residence times (Siebler et al., 2019) and especially the locations of compartment barriers, volume flow exchange rates (Vrábel et al., 2000, 1999) and respective mixing times (Rosseburg et al., 2018) provide fundamental information to the implementation of a scale-down model (Gaugler et al., 2022; Noorman, 2011).

On industrial scale, aforementioned hydrodynamic process data can be typically obtained by means of two basic sensor measurement approaches: The Eulerian approach, which is the industrial standard, utilizes locally fixed probes, either at one specific position at the reactor wall or multiple probes distributed over the height or circumference of the reactor. The collected data delivers quasi-1-dimensional information about fermentation process conditions, such as temperature, pH, dissolved oxygen concentration or conductivity (Gargalo et al., 2020) over time. However, with these sensor types, neither the cell's duration of residence in individual metabolic regimes nor gradients can be resolved spatiotemporally. Only a coarse and locally constrained data density can be obtained, thus making it insufficient to deliver adequate values for scale-down reactor models. The Lagrangian approach is based on particles submersed in a liquid, which follow the fluid flow in a characteristic manner, depending on their physical properties. Through the implementation of multiple sensor systems within an inertial, finite-sized, mostly neutrally buoyant and freely moving Lagrangian Sensor Particle (LSP) (Fitschen et al., 2023; Buntkiel et al., 2023a), the primary objective is to understand cell-bioreactor interactions, while mimicking the movement of a cell. This 3-dimensional concept "Traveling along the Lifelines of Single Cells" in a stirred bioreactor was introduced by Lapin et al. (2004) and recently reviewed by Blöbaum et al. (2023) for both experimental and numerical methods. Regarding the latter, Haringa et al. (2016) have demonstrated an approach to gain statistical insights into metabolic regime analyses,

eventually allowing for a quantification of substrate concentration variations with regard to scale-down models. This Lagrangian regime analysis, further investigated in following studies (Kuschel and Takors, 2020; Haringa et al., 2017, 2018), can depict frequency and magnitude statistics of environmental fluctuations in compartmentalized flows. However, experimental data is still required in order to further calibrate compartment models (Nadal-Rey et al., 2021a; Delafosse et al., 2014) and validate Lagrangian particle simulations (Hofmann et al., 2022; Kuschel et al., 2021).

Initial investigations regarding the utilization of active flow-followers for analyzing circulation times and their correlation to mixing times in a STR were conducted by Bryant and Sadeghzadeh (1979). Day (1975) discussed a log-normal distribution of measured circulation times with the same flow-followers. In addition, model parameters like the non-dimensional flow number and mixing times were validated. Their work is based on the development of "radio pills" by Mitchell (1969). Moreover, Middleton (1979) and Van Barneveld et al. (1987a,b) continued circulation time measurements in large-scale STRs of up to 20 m^3, whereas Mann et al. (1981) focused on a stochastic flow model utilizing the respective data and emphasizing the careful interpretation of circulation time distributions (CTD) with regards to their length of experiments. In the past decades, a large number of research groups have continued investigating the application of LSPs in the context of biotechnology (Reinecke et al., 2012; Bisgaard et al., 2021b,a, 2020; Buntkiel et al., 2023b; Lauterbach et al., 2019; Reinecke et al., 2022; Stine et al., 2020b,a; Todtenberg et al., 2015), however, their application in industrial-scale STRs is rarely published.

Whereas Reinecke et al. used a single-staged pitched blade turbine (PBT) in STRs with volumes between 0.8 and 1.4 m^3 (Reinecke et al., 2012; Reinecke, 2013), Bisgaard et al. (2021a) applied their LSPs in STRs with approx. 0.6 m^3 and studied both a single-stage PBT and a single-stage Rushton turbine (RT) setup. Apart from these well-known impeller configurations, particularly for mammalian cell cultivations (Sieck et al., 2013), plant cell suspension cultures (O'Neill et al., 2008) or β-cell spheroid productions (Petry and Salzig, 2022), Elephant Ear (EE) impellers are widely utilized in STRs due to their enhanced bulk mixing characteristic attributed to a wide blade shape and a high impeller-to-reactor diameter ratio ($d_{imp}\, d_{STR}^{-1} \approx 0.5$). Nevertheless, in literature, this 3-bladed, 45° pitched impeller with a predominant axial flow direction has not been reported as of 2006 (Nienow, 2006) and since then mainly in two variations, named as the *Applikon* design (Collignon et al., 2010a,b; Delbridge et al., 2023; Rotondi et al., 2021; Simmons et al., 2007; Zhu et al., 2009) and the *ABEC* design (O'Neill et al., 2008; Petry and Salzig, 2022; Fitschen, 2021; Meier, 2005). Nonetheless, no mixing study, which considers a three-staged EE impeller *ABEC* design on industrial scale in a baffled STR has been published to date.

In that context, this study focuses on aforementioned issues and combines (i) the application of LSPs in a baffled 15,000 L STR, which is (ii) equipped with three EE impellers (*ABEC* design) in order to (iii) gather experimental data regarding circulation times and residence times, based on the calculation of the vertical probability of presence and axial velocities to localize compartments, compare these results with global mixing times for the same setup and conduct a Lagrangian single-phase hydrodynamic regime analysis. Moreover, dimensionless numbers as the Stokes number and different Flow numbers are estimated and compared to literature findings.

2. Materials and methods

In this section, the reactor setup and Lagrangian Sensor Particles (LSP) are described in detail. The description of pressure data evaluation is provided, meaning the calculation of the vertical probability of presence, determining the circulation time distribution, and calculating the hydraulic residence time distribution. Moreover, the experimental method for measuring the global mixing times in the aforementioned reactor and the approaches for estimating the Stokes number and different Flow numbers are described.

Table 1
Overview of system parameters in deionized water and isotonic solution.

	Deionized water (DW)	Isotonic solution (IS)
Temperature T/°C	(22 ± 0.3)	(37.0 ± 0.3)
Dynamic viscosity η/ Pa s ($\cdot 10^{-3}$)	0.95	0.71
Fluid density ρ_f/ kg m^{-3}	(997.8 ± 0.4)	(1007.7 ± 0.4)
LSP density ρ_p/ kg m^{-3}	$\rho_f \leq \rho_p \leq (\rho_f + 2)$	$(\rho_f - 1) \leq \rho_p \leq (\rho_f + 2)$
Archimedes number Ar ($\cdot 10^3$)/–	≤ 1.38	≤ 1.78

2.1. 15,000 L acrylic glass bioreactor and Elephant Ear impellers

For this study, a transparent acrylic glass bioreactor with an inner diameter of $d_{STR} = 2.0$ m, a filling level of $H = 4.2$ m and a klöpper head is characterized hydrodynamically (Fig. 1). The reactor has been erected in cooperation with Boehringer Ingelheim Pharma GmbH & Co. KG (Rosseburg et al., 2018). The total working volume is $V = 12500$ L of either deionized water (DW) at a temperature of $T = (22 \pm 0.3)$ °C or an isotonic solution (IS) with sodium chloride ($c_{NaCl} = 9$ g L^{-1}) at a temperature of $T = (37 \pm 0.3)$ °C. The fluid densities are measured with $\rho_f = (998.0 \pm 0.4)$ kg m^{-3} and $\rho_f = (1007.7 \pm 0.4)$ kg m^{-3} (Anton Paar DMA 4500 M) and the corresponding dynamic viscosities are estimated with $\eta = 0.95 \cdot 10^{-3}$ Pa s and $\eta = 0.71 \cdot 10^{-3}$ Pa s, respectively. The reactor is equipped with four equally spaced baffles of width $b = 0.1 \cdot d_{STR}$ and a bottom-driven magnetic agitator (ZETA BMRF XXL) with three Elephant Ear (EE) impellers having a diameter $d_{imp} = 0.915$ m, which corresponds to a ratio of $d_{imp}\, d_{STR}^{-1} = 0.46$. The off-bottom clearance $C = 0.3 \cdot d_{STR}$ and an impeller spacing of $h\, d_{imp}^{-1} = 1.0$. Applied stirring frequencies range from $n = 15$ rpm (corresponds to $u_{tip} = 0.72$ m s^{-1}) to $n = 40$ rpm (corresponds to $u_{tip} = 1.9$ m s^{-1}) (see Table 2).

With an estimated Power number of $Po = 5.3$ for this setup, the global volumetric power inputs

$$\frac{P}{V} = \frac{Po \cdot \rho_f \cdot n^3 \cdot d_{imp}^5}{V} \tag{1}$$

and stirrer Reynolds numbers

$$Re_{STR} = \frac{n \cdot d_{imp}^2 \cdot \rho_f}{\eta} \tag{2}$$

are mentioned in Table 2 for each respective medium. Furthermore, with those values, the mean specific energy dissipation rate $\bar{\varepsilon}_T$ and the Kolmogorov length scale λ_K can be derived according to

$$\bar{\varepsilon}_T = \frac{P}{V \rho_f} \tag{3}$$

and

$$\lambda_K = \left(\frac{\nu^3}{\bar{\varepsilon}_T} \right)^{\frac{1}{4}}, \tag{4}$$

where ν denotes the kinematic viscosity of the fluid. Since the energy dissipation rate varies throughout the STR and is highest in the discharge flow of the impellers, a ratio of $\Phi = (\varepsilon_T)_{max} (\bar{\varepsilon}_T)^{-1} = 115$ is estimated for the respective region (Ståhl Wernersson and Trägårdh, 1999) according to

$$\log(\Phi) = -1.04 \cdot \frac{2r}{d_{imp}} + 3.1, \tag{5}$$

with r as the radial distance from the bioreactor center line. The smallest scale of turbulence is found at $2r\, d_{imp}^{-1} = 1$, resulting in a decrease of Φ with increasing distance to the impeller tip. Moreover, Φ varies substantially with the impeller-to-reactor diameter ratio $d_{imp}\, d_{STR}^{-1}$, but less with the impeller type (Nienow, 2021). It is most importantly independent of scale and also found in literature with lower values as 100, 40 or approx. 14 (Nienow et al., 2013; Sieck et al., 2013; Nienow,

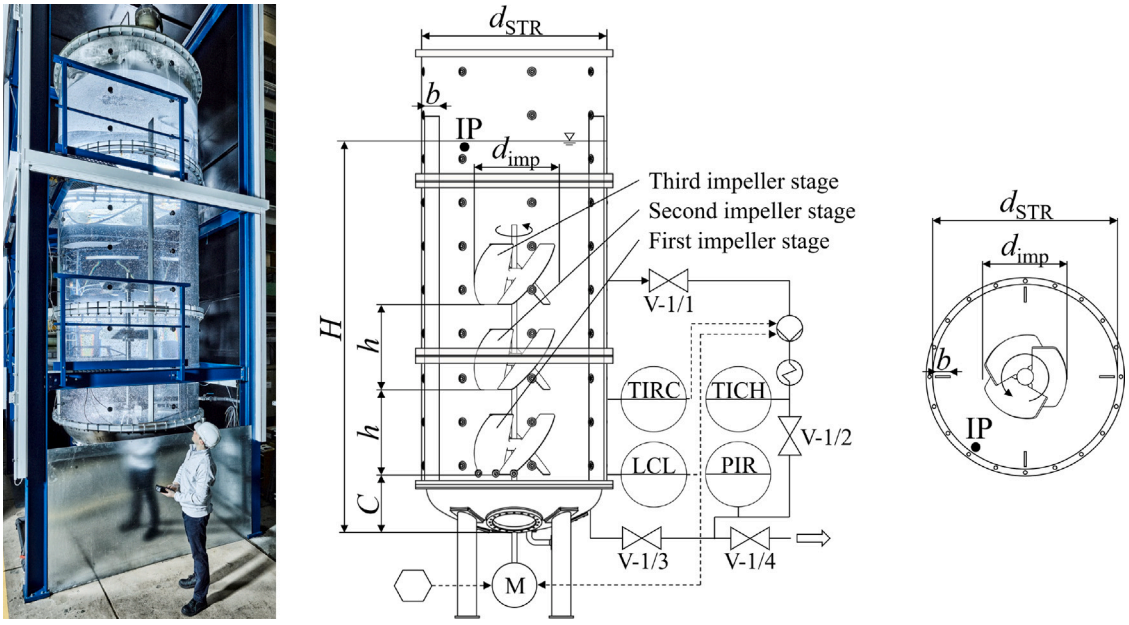

Fig. 1. Schematic overview of the acrylic glass reactor with a filling level H, a diameter d_{STR}, equipped with baffles with a width b. Three Elephant Ear (EE) impellers with a diameter d_{imp} are installed with a spacing h and an off-bottom clearance C. Valves V-1/1, V-1/2 and V-1/3 build a closed loop when heating the reactor. Valve V-1/4 is used to take a sample. Temperature (T), level (L) and pressure (P) are controlled (C), recorded (R) or indicated (I) via static probes. The location of the injection point (IP) for hydrochloric acid for the mixing time experiments is indicated with a black dot.

Table 2
Overview of stirrer Reynolds numbers Re_{STR}, volumetric power inputs PV^{-1}, Kolmogorov length scales λ_K, estimated minimum Kolmogorov length scales in the vicinity of the impeller tip $\lambda_{K,\Phi=115}$ and estimated Taylor scales L_E for both medium types, deionized water (DW) and isotonic solution (IS).

Medium	Mixing parameter	Impeller frequency n/rpm					
		15	20	25	30	35	40
DW	Re_{STR} $(\cdot 10^5)$/–	2.2	2.9	3.7	4.4	5.1	5.9
	PV^{-1}/W m^{-3}	4.2	10.0	19.6	33.9	53.9	80.4
	λ_K $(\cdot 10^{-6})$/m	119.4	96.2	81.4	71.0	63.2	57.2
	$\lambda_{K,\Phi=115}$ $(\cdot 10^{-6})$/m	36.5	29.4	24.9	21.7	19.3	17.5
	L_E $(\cdot 10^{-3})$/m	41.7	36.1	32.3	29.5	27.3	25.5
IS	Re_{STR} $(\cdot 10^5)$/–	3.0	4.0	5.0	5.9	6.9	7.9
	PV^{-1}/W m^{-3}	4.3	10.1	19.8	34.3	54.4	81.2
	λ_K $(\cdot 10^{-6})$/m	95.3	76.8	64.9	56.6	50.5	45.6
	$\lambda_{K,\Phi=115}$ $(\cdot 10^{-6})$/m	29.1	23.5	19.8	17.3	15.4	13.9
	L_E $(\cdot 10^{-3})$/m	35.8	31.0	27.8	25.3	23.5	21.9

2021). According to previous studies, no cell damage is likely to occur in the STR utilized herein, since almost all estimated Kolmogorov scales $\lambda_{K,\Phi=115}$ are greater than estimated mammalian cell sizes (CHO cell sizes range between 12 µm and 14 µm) and smaller than those reported in literature (Nienow, 2006, 2021; Nienow et al., 2016; Nienow, 2014).

2.2. Lagrangian Sensor Particles

2.2.1. Hardware components

The Lagrangian Sensor Particles (LSPs), developed by the Helmholtz-Zentrum Dresden-Rossendorf (HZDR), have a diameter of d_{LSP} = 40 mm, carry an approx. weight of m_{LSP} = 33 g and consist of two half-shells, which are connected by a threaded rod and sealed with an O-ring (Fig. 2). Hardware and electronic components are described by Buntkiel et al. (2023a,b), while this study solely makes use of the pressure sensor data at a sample rate of approx. f = 50 Hz. For each stirring speed, four LSP datasets are considered, whereby two originate from a separate trial accounting for a total measurement time of at least 245 min (Hofmann et al., 2023).

For the experiments presented, two temperatures ($T \in \{20, 37\}$ °C), and thus respective medium properties (DW and IS) are covered (Table 1) to match and demonstrate the technical feasibility for the LSPs during generic fermentation conditions. Therefore, the rpm cases $n \in \{15, 25, 35\}$ rpm are evaluated in DW at T = 20 °C, and $n \in \{20, 30, 40\}$ rpm are evaluated in IS at T = 37 °C. In order to be able to compare both datasets quantitatively, the 35 rpm case is evaluated and compared for both conditions and temperatures.

2.2.2. Density calibration

In order to calibrate the LSP densities for each trial, two glass vessels are prepared. As a reference, the first contains the reactor media, obtained from the bottom valve V-1/4. The second one contains also reactor medium, however, is adjusted with additional sodium chloride to match the upper limit of the allowed density range (see Table 1). By submerging the vessels in a water bath, they are kept at the same temperature as the respective reactor medium. If an LSP sinks in the first vessel and surfaces in the second vessel, the LSP's density fulfills the criteria and is used for the trial. If this is not the case, the LSP's density is adjusted by turning the upper half shell, consequently increasing or decreasing the LSP's volume.

2.3. Stokes number estimations

Previous studies (Hofmann et al., 2022; Bisgaard et al., 2021a) utilize the Stokes number St as a characteristic dimensionless number to estimate the flow-following capability of an LSP with regard to the surrounding fluid flow. Findings in literature indicate that a particle can serve as an effective flow-follower if the magnitude of the Stokes number $St \sim \mathcal{O}(10^{-2})$ is met, particularly when investigating single-point flow statistics (Ouellette et al., 2008). Additionally, Tropea et al. (2007) suggest that if $St < 0.1$, the respective particle yields an acceptable level of accuracy in flow tracing, resulting in errors of less than 1 %. Generally, the Stokes number

$$St = \frac{\tau_p}{\tau_f} \tag{6}$$

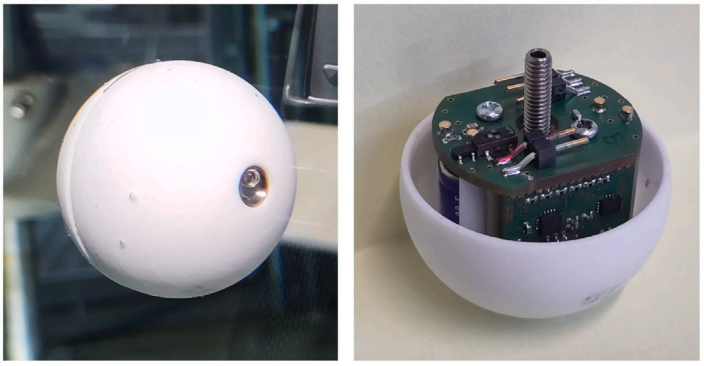

Fig. 2. Closed LSP in a tank (left) and open LSP with hardware components and threaded rod (right) (Buntkiel et al., 2023a).

is defined as the ratio of the particle response time τ_p to the temporal scale of change of the fluid velocity τ_f (Crowe et al., 2011). Based on the single equations for

$$\tau_p = \frac{4}{3}\frac{\rho_p d_p^2}{\eta c_D Re_p}, \tag{7}$$

with ρ_p being the particle density, d_p the particle diameter, η the dynamic viscosity, c_D the drag coefficient according Haider and Levenspiel (Haider and Levenspiel, 1989) (using the four-parameter general drag correlation for a sphere with a sphericity $\phi = 1$), the particle Reynolds number

$$Re_p = \frac{\rho_f d_p |u - v|}{\eta}, \tag{8}$$

which considers the difference between the fluid velocity u and the particle velocity v, and

$$\tau_f = \frac{L}{u}, \tag{9}$$

where L is a characteristic fluid flow length scale, the equation

$$St = \frac{4}{3}\frac{\rho_p}{\rho_f}\frac{d_p}{|u - v|\, c_D}\frac{u}{L} \tag{10}$$

can be derived.

Regarding the definition of τ_f, instead of using $L = d_{imp}$ as proposed by Reinecke et al. (2012), which contemplates the meso-scale of the mixing process, but would, however, underestimate the Stokes number as demonstrated by Hofmann et al. (2022), this study makes use of the approach that $L = L_E$ with the Taylor scale

$$L_E = u_0\sqrt{\frac{15\nu}{\bar{\varepsilon}_T}} \tag{11}$$

to cover the Stokes number estimation on the micro-scale. Therein, ν is the kinematic viscosity and u_0, defined as the root-mean-square of the fluid velocity (Huilier, 2021), is in this case estimated as the tip speed u_{tip}. Moreover, as described in Reinecke et al. the fluid velocity u is estimated as the tip speed u_{tip} so that

$$St = \frac{4}{3}\frac{\rho_p}{\rho_f}\frac{d_p}{\left(u_{tip} - |\overline{v}|_{z,max}\right) c_D}\sqrt{\frac{\bar{\varepsilon}_T}{15\nu}} \tag{12}$$

is derived, where $|\overline{v}|_{z,max}$ is the maximum average axial LSP velocity for the respective impeller frequency at height z. This approach covers especially the most turbulent region near the impeller tip, whereas the Stokes number for the macro-scale can be represented if the overall circulation time is considered as $\tau_f = \bar{t}_{circ,overall}$ (Reinecke et al., 2012).

2.4. Vertical probability of presence and axial velocities

After assessing the flow-following capability of the LSPs in the utilized reactor volume, the vertical probability of presence and axial velocities are calculated. To do so, the vertical position of an LSP is obtained by its hydrostatic pressure measurement by applying Pascal's law

$$z(t) = H - \frac{p(t) - p_0}{\rho_f\, g}, \tag{13}$$

where $z(t)$ is the LSP's height at a point in time, H is set as the filling level of the reactor, $p(t)$ is the measured pressure at a point in time, p_0 is the measured ambient pressure before each trial for each LSP, ρ_f is the density of the respective fluid and g the gravitational acceleration. All evaluated raw data is pre-processed with a low-pass filter and interpolated afterwards. For this purpose, a *moving average* of five consecutive values and a *spline* interpolation to obtain a uniform 50 Hz signal are used, respectively. For further analyses, the reactor is divided into 42 equally distributed vertical reactor volumes j with a respective height of $h_j = 0.1$ m.

The vertical probability of presence P is generally calculated in relative percentage as

$$P_j = 100 \cdot \frac{N_j}{M} \tag{14}$$

with N_j being the number of counts in the respective bin j and M being the total number of counts in the dataset.

The LSP's axial velocity $v_z(t)$ is the time derivative of the LSP's vertical position with respect to the interpolated 50 Hz ($dt = 20$ ms) signal as

$$v_z(t) = \frac{dz(t)}{dt}. \tag{15}$$

The velocity can be distinguished between positive $v_{z,pos}(t)$ (upwards movement) and negative $v_{z,neg}(t)$ (downwards movement) velocity. For each, average values and corresponding uncertainties Δ are generally calculated as

$$\Delta_{\overline{x}} = \sqrt{\frac{1}{N(N-1)}\sum_{i=1}^{N}(x_i - \overline{x})^2} \tag{16}$$

with N being the sample size and $\overline{x}$ the average value. Due to differing amounts of initially obtained data points per dataset, a weighted average with a corresponding error propagation is calculated and plotted.

2.5. Determination of circulation time distributions

The tracer injection method stands as the predominant approach for acquiring circulation times and specifically mixing times. This method involves introducing a tracer substance into the liquid, followed by the analysis of the rate at which uniform blending occurs. However, in order to attain detailed information about dead zones, overall flow structures, and the probability density of the circulation time distribution (CTD) more information is required. This is the reason why the pressure sensor data of LSPs is utilized. In previous publications, only one reactor height was chosen to determine a CTD, either with a

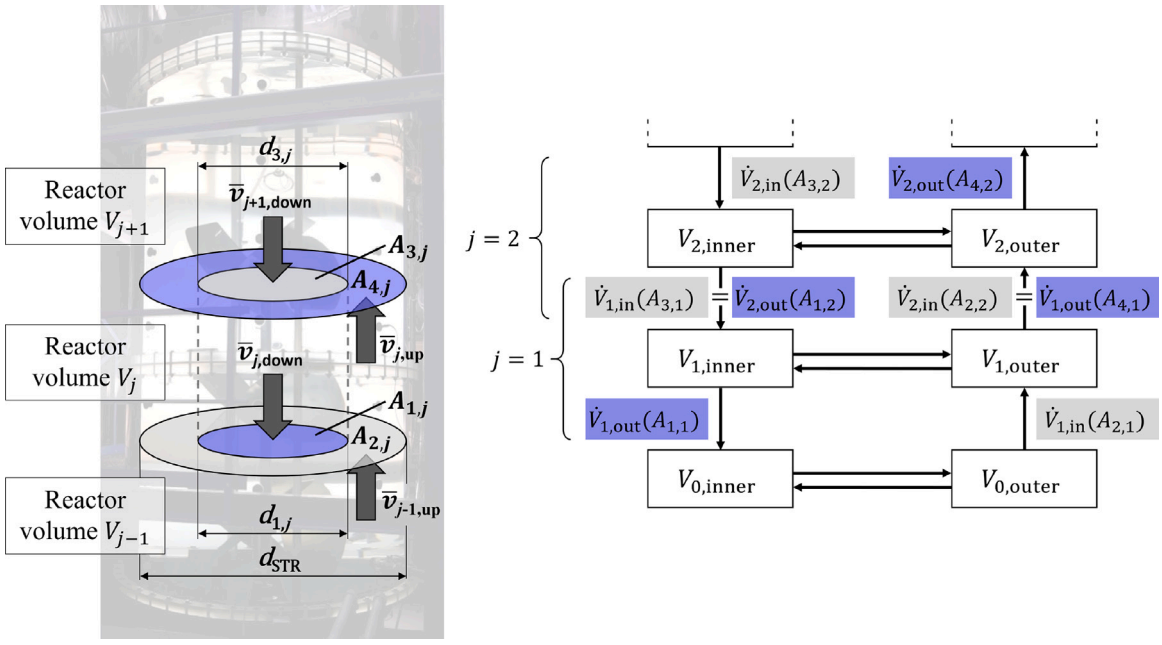

Fig. 3. Schematic depiction of the residence time modeling approach and the coherence between the respective reactor volumes and their volume flow rates.

physically installed aerial ring (Middleton, 1979) or deliberately chosen at the height of the impeller (Bisgaard et al., 2021a). However, in order to hydrodynamically characterize the entire reactor and determine compartments, an overall picture is required and herein evaluated. Hence, CTDs are obtained for each reactor slice j over the entire reactor height H (Reinecke, 2013).

To do so, as previously described, the reactor is divided into 42 equally distributed vertical reactor volumes j with their vertical central plane. If an LSP crosses a respective central plane at $t = 0$ from top to bottom, the signal is recorded as $t_{\text{circ},j,t=0}$. Once it crosses that plane the second time from top to bottom with the signal $t_{\text{circ},j,t>0}$, the time difference $t_{\text{circ},j,\text{dt}}$ is referred to one circulation time value per plane j. This method yields a distribution for all reactor planes and discloses axial hydrodynamic compartments throughout the reactor.

2.6. Determination of residence time distributions

In order to reveal the hydraulic residence time distributions and present a second approach to distinguish hydrodynamic compartments within the reactor, several assumptions are made, based on the descriptions in Fig. 3:

(i) Although the reactor is equipped with a dished head, it is assumed to be an overall cylinder with a surface area of $A = 3.14\ \text{m}^2$. With the height of $h_j = 0.1$ m each volume amounts to $V_j = 0.314\ \text{m}^3$.

(ii) Due to the predominant axial flow direction of the EE impellers, in each reactor volume V_j, an inner volume $V_{j,\text{inner}}$ and an outer volume $V_{j,\text{outer}}$ is assumed, which shows a downflow and an upflow behavior, respectively. Hence, each individually recorded LSP velocity data point within a reactor volume is allocated either to the inner volume as $v_{j,\text{down}}$, if it shows a negative value (meaning positive pressure change over time), or allocated to the outer volume as $v_{j,\text{up}}$, if it shows a positive value (meaning negative pressure change over time). For each reactor volume, respective weighted time averaged values $\overline{v}_{j,\text{down}}$ and $\overline{v}_{j,\text{up}}$ are determined.

(iii) Each reactor volume has a lower boundary ($A_{\text{STR}} = A_{1,j} + A_{2,j}$) and an upper boundary ($A_{\text{STR}} = A_{3,j} + A_{4,j}$), which are defined respectively as

$$A_{1,j} = \frac{\pi}{4} \cdot d_{1,j}^2;\ A_{2,j} = \frac{\pi}{4}(d_{\text{STR}}^2 - d_{1,j}^2) \tag{17}$$

$$A_{3,j} = \frac{\pi}{4} \cdot d_{3,j}^2; A_{4,j} = \frac{\pi}{4}(d_{\text{STR}}^2 - d_{3,j}^2), \tag{18}$$

where $A_{1,j}$ and $A_{3,j}$ can be different. Therefore, depending on their respective size, the inner volume $V_{j,\text{inner}}$ has either a cylindrical or a tapered shape.

(iv) Due to mass conservation $\text{d}\rho\ \text{d}t^{-1} = \text{const.}$, it can be generally concluded that the volume flow into a reactor volume $\dot{V}_{j,\text{in}}$ must be equal to the volume flow out of that volume $\dot{V}_{j,\text{out}}$ as

$$\dot{V}_{j,\text{in}} = \dot{V}_{j,\text{out}}, \tag{19}$$

where they can be calculated as

$$\dot{V}_{j,\text{in}} = |\overline{v}|_{j+1,\text{down}} \cdot A_{3,j} + \overline{v}_{j-1,\text{up}} \cdot A_{2,j} \tag{20}$$

$$\dot{V}_{j,\text{out}} = |\overline{v}|_{j,\text{down}} \cdot A_{1,j} + \overline{v}_{j,\text{up}} \cdot A_{4,j}, \tag{21}$$

leading to

$$|\overline{v}|_{j+1,\text{down}} \cdot A_{3,j} + \overline{v}_{j-1,\text{up}} \cdot \frac{\pi}{4}(d_{\text{STR}}^2 - d_{1,j}^2) = |\overline{v}|_{j,\text{down}} \cdot A_{1,j} + \overline{v}_{j,\text{up}} \cdot \frac{\pi}{4}(d_{\text{STR}}^2 - d_{3,j}^2). \tag{22}$$

Since d_1 and d_3 are unknown, an iteration takes place, which starts with the lowest reactor volume and an assumed start value for d_1. Consequently, d_3 can be calculated as

$$d_{3,j} = \sqrt{\frac{d_{1,j}^2 \cdot (|\overline{v}|_{j,\text{down}} + \overline{v}_{j-1,\text{up}}) + d_{\text{STR}}^2 \cdot (\overline{v}_{j,\text{up}} - \overline{v}_{j-1,\text{up}})}{|\overline{v}|_{j+1,\text{down}} + \overline{v}_{j,\text{up}}}}. \tag{23}$$

(v) With continuing the calculation of the respective diameters for $j = 1$ towards the next reactor volume $j = 2$ and so forth (see Fig. 3), the previously calculated value for $d_3(j = 1)$ must be equal to $d_1(j = 2)$. Hence, the calculated top surface area (e.g. $A_{3,1}$) from the previous step must be equal to the bottom surface area (e.g. $A_{1,2}$) in the current step as

$$d_{3,j} = d_{1,j+1} \Leftrightarrow A_{3,j} = A_{1,j+1} \tag{24}$$

(vi) If Eq. (19) is not met, the iteration process restarts at the lowest reactor volume. The start value is preset to $d_1 = 0.20$ m, the iteration step width is set at 0.01 m, and the maximum value $d_1 = 1.80$ m. If an iteration loop ends successfully with the upmost possible reactor volume $V_{j=40}$, the values are saved.

(vii) There is a possibility that side flows can occur, and thus the inner and outer volumes in a reactor volume j can exchange mass. Furthermore, as a boundary condition, the lowermost volume $j = 0$ and the topmost volume $j = 41$ do neither interact with the dished head of the reactor nor with the gas volume above the liquid surface, respectively.

Eventually, based on those results, inner and outer volume flows for each reactor volume can be calculated as

$$\overline{\dot{V}}_{j,\text{inner}} = |\overline{v}|_{j+1,\text{down}} \cdot \overline{A}_{3,j}, \tag{25}$$

$$\overline{\dot{V}}_{j,\text{outer}} = \overline{v}_{j-1,\text{up}} \cdot \overline{A}_{2,j}, \tag{26}$$

which is finally checked for the overall mass conservation criteria, meaning

$$\sum_{j=1}^{40} \dot{V}_{j,\text{inner}} \approx \sum_{j=1}^{40} \dot{V}_{j,\text{outer}}. \tag{27}$$

If this is the case, the respective volume flows are taken into account for an average value and the respective uncertainty calculated on error propagation, leading to the respective hydraulic residence times as

$$\overline{\tau}_{j,\text{inner}} = \frac{\overline{V}_{j,\text{inner}}}{\overline{\dot{V}}_{j,\text{inner}}} \quad \text{and} \quad \overline{\tau}_{j,\text{outer}} = \frac{\overline{V}_{j,\text{outer}}}{\overline{\dot{V}}_{j,\text{outer}}}. \tag{28}$$

For an additional assessment, respective residence times are added up to calculate the overall average hydraulic residence time as

$$\overline{\tau}_{\text{overall}} = \sum_{j=1}^{40} \overline{\tau}_{j,\text{inner}} + \sum_{j=1}^{40} \overline{\tau}_{j,\text{outer}}. \tag{29}$$

This approach treats the STR as if it would be consisting of two interconnected plug flow reactors for the inner and for the outer volume flow, respectively.

2.7. Compartment determination and Lagrangian regime analysis

Based on previously described calculations, hydrodynamic compartments are determined for both the circulation time and residence time distributions. To do so, in order to present a quantitative approach, the respective circulation time and residence time trends are first smoothed with a *moving average* of five consecutive values. Afterwards, each single value for the reactor slice j in a trend is compared with the values $j-2$ and $j+2$ in the same trend. A deliberate cut-off factor of 2.3 shows the best fitting results for the investigated rpm cases, to depict a division between centrally located rather low values and comparatively high values at the top and bottom of the reactor.

The primary difficulty accompanied with scale-down simulators lies in creating a simulator on laboratory scale, which accurately replicates the conditions of the industrial process (Gaugler et al., 2022; Neubauer and Junne, 2016). Presently, microbial lifelines (Lapin et al., 2004, 2006) are primarily obtained by means of computational fluid dynamic models. Blöbaum et al. (2023) reviewed these concepts critically and describe therein an approach of Haringa et al. where different Euler–Lagrange analysis methods are utilized to gain insight about metabolic dynamics in fermentation processes on industrial scales (Haringa et al., 2017, 2018; Haringa, 2023). Based on numerically determined lifelines in a domain with three zones, in which different metabolic responses occur, a metabolic Lagrangian regime analysis offers valuable information about the average regime residence time of cells. This can be further used to adjust a scale-down simulator. This study, however, comprises the hydrodynamic Lagrangian regime analysis with obtained LSP data by encompassing on the one hand the calculated axial locations of the hydrodynamic compartment barriers, based on the circulation time distribution results, for the respective rpm case. On the other hand, the LSP's Lagrangian axial lifeline over time $h(t)$ is utilized. Similar to the approach by Haringa et al. (2018), a residence time distribution per hydrodynamic regime (in this study: upper, center and lower) is obtained for any LSP lifeline. Hence, a percentage of cells exposed to theoretical oxygen deprivation conditions in the upper compartment can be derived, although this study only utilizes and analyses the single-phase hydrodynamics.

2.8. Mixing time measurements

The global mixing time $t_{\text{mix,global,95}}$ is determined experimentally (Fitschen et al., 2021b) in the same reactor by means of the decoloration method utilizing bromothymol blue (BTB) and the addition of a 2 M hydrochloric acid (HCl) and a 2 M sodium hydroxide (NaOH) solution in DW at $T = 37\,°\text{C}$. Initially, a $30\,\text{g}\,\text{L}^{-1}$ BTB solution in 99.9 v/v-% Ethanol is prepared, of which 100 mL is added into the reactor volume. Prior to each measurement, pH is first adjusted to $7.0 < \text{pH} < 7.5$ and checked with a WTW SenTix 41-3 probe, which corresponds to a green color. Consequently, 250 mL of the NaOH solution is added in order to gain a color shift to blue. After this preparation step, 500 mL of HCl solution is pneumatically introduced from a storage tank (1.2 m above the water surface) into the reactor to achieve a color shift to yellow via green. Afterwards, the storage tank is rinsed with DW. Simultaneously, as an indicator to start the measurement, the background illumination is switched on at the moment of the addition (Rosseburg et al., 2018). The injection point (IP, see Fig. 1) is located at a distance of 0.1 m from the reactor wall and 35° before the baffle in rotational direction of the impeller blades. The injection of HCl takes 3 s and is performed 0.2 m beneath the water surface through a vertically installed diffusor nozzle outlet with a diameter of 30 mm and a height of 50 mm. Uniform lighting condition is provided by five spotlights, four white LED panels and a white diffuser foil, which is located behind the reactor. The decoloration is recorded at a sampling rate of 50 Hz by a NIKON D7500 with a SIGMA lens (1:1.8, 20 mm f/22.0) at a resolution of 1920 x 1080 pixels at a height of 0.9 m above the lowest point of the reactor and a distance of 5.1 m to the impeller shaft. The mixing is quantitatively analyzed with an in-house developed open-source MATLAB algorithm (Fitschen et al., 2021a) utilizing the evolution of the gray values over time. The global mixing time is defined as the duration starting from the HCl solution addition until the normalized mean gray value attains 95 % of the final value (Rosseburg et al., 2018). Each experiment is repeated three times at each $n \in \{16, 21, 29, 37, 40\}$ rpm.

2.9. Flow number estimations

Furthermore, in order to characterize a specific impeller type, describe the flow phenomena in an STR and provide crucial parameters for modeling, four different Flow numbers are estimated and introduced in this study: (i) the Pumping number $N_{\text{Q,p}}$, (ii) the Circulation Flow number $N_{\text{Q,c}}$, (iii) the Residence Flow number $N_{\text{Q,r}}$ and (iv) the Exchange Flow number $N_{\text{Q,e}}$ (Vrábel et al., 2000, 1999; Nienow, 1998; Schubert, 2008). The Residence Flow number is not found in literature and introduced herein as a measure to describe the overall flow of LSPs in the STR. Being independent of the impeller frequency in the turbulent regime, they proof to be valuable for process scaling.

(i) The Pumping number $N_{\text{Q,p}}$ for an axial down-pumping impeller is generally calculated by the swept volume flow Q_{p} through the impeller zone d_{imp} (Tatterson, 1991) at the impeller frequency n as

$$N_{\text{Q,p}} = \frac{Q_{\text{p}}}{n \cdot d_{\text{imp}}^3}. \tag{30}$$

(ii) The circulation volume flow Q_{c} considers an additional entrained flow (Schubert, 2008). It is influenced by the introduction of the overall momentum flow into the fluid and utilizes the average circulation rate in the whole path (Vrábel et al., 1999). In case of

a single-phase flow as investigated in this study, the Circulation Flow number is defined as

$$N_{\mathrm{Q,c}} = \frac{Q_{\mathrm{c}}}{n \cdot d_{\mathrm{imp}}^3}. \tag{31}$$

As an approximation, the reactor volume V is pumped within an average circulation time $\bar{t}_{\mathrm{circ}}$, which is described by

$$\bar{t}_{\mathrm{circ}} = \frac{V}{Q_{\mathrm{c}}} \tag{32}$$

and consequently, both Eqs. (30) and (31) yield the expression

$$\frac{1}{\bar{t}_{\mathrm{circ}}} = \underbrace{\frac{N_{\mathrm{Q,c}} \cdot d_{\mathrm{imp}}^3}{V}}_{k_{\mathrm{to}}} \cdot n = k_{\mathrm{to}} \cdot n, \tag{33}$$

meaning the average circulation time is inversely proportional to the impeller frequency ($\bar{t}_{\mathrm{circ}}^{-1} \propto n$) (Middleton, 1979). This plot reveals the turn-over constant k_{to} as the slope, after which $N_{\mathrm{Q,c}}$ is derived.

(iii) To calculate the Residence Flow number $N_{\mathrm{Q,r}}$ the same approach is used, however, instead of taking the average circulation time into account, all residence times $\tau_{j,\mathrm{inner}}$ and $\tau_{j,\mathrm{outer}}$ are added up to obtain the total turn-over time.

(iv) The Exchange Flow number

$$N_{\mathrm{Q,e}} = \frac{Q_e}{n \cdot d_{\mathrm{imp}}^3} \tag{34}$$

describes the exchange flow rate Q_{e} as a result of the flow driven by turbulence across the cross-sectional area of the reactor (Vrábel et al., 2000). Hence, it specifies the magnitude of fluid exchanged between neighboring compartments in axial direction (Vrábel et al., 1999). Since volume flows are determined in the course of the residence time calculations, this Flow number can be directly calculated for different reactor heights without a reciprocal regression.

3. Results and discussion

In this chapter, the evaluation of the pressure sensor data is described, depicted and discussed. According to the calculations explained in the previous chapter, the Lagrangian Sensor Particle's (LSP) vertical probability of presence, their resulting axial velocity in the reactor and their corresponding circulation time and residence time distribution is presented in order to determine hydrodynamic compartments. Moreover, a Lagrangian regime analysis is presented to estimate potential oxygen depletion periods for CHO cells on industrial scale. Dimensionless numbers as the Stokes number and different Flow numbers are estimated to put the results in context with literature. Eventually, measured global mixing times in the same reactor are compared to previously acquired results and literature correlations.

3.1. Stokes number estimations

In order to estimate and eventually compare the flow-following capability of the LSPs used in this study by means of the Stokes number St, calculation approaches are suggested in Section 2.3. The values for the micro-scale in the vicinity of the EE impellers are estimated as $St \in \{4.0, 4.7, 5.1, 5.4, 5.7, 6.2\}$ for the experiments in DW and $St \in \{4.5, 5.3, 5.9, 6.2, 6.6, 7.2\}$ for the experiments in IS for all impeller frequencies, respectively. Regarding the Stokes number for the meso-scale, values are between $0.17 < St < 0.18$ and for the macro-scale $St \approx 0.004$ (see Table 4). Considering the results described by van Van Barneveld et al. (1987a,b), Reinecke et al. (2012) and Bisgaard et al. (2021a), this study's Stokes numbers are in a similar range.

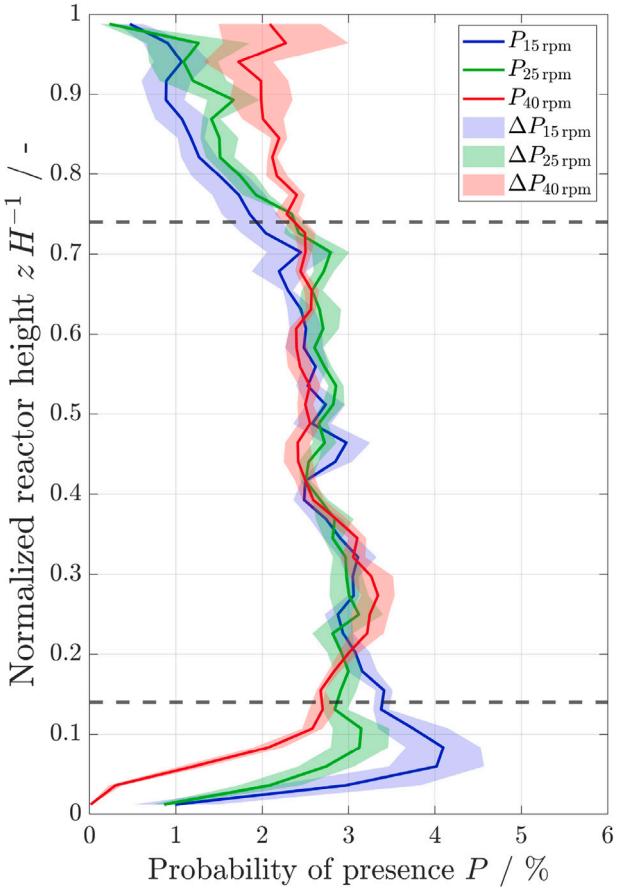

Fig. 4. Axial probability of presence over the normalized reactor height ($H = 4.2$ m) for four LSP data sets for each impeller frequency of 15 (blue line), 25 (green line) and 40 rpm (red line) for a vertical bin size of 10 cm. Shaded areas show uncertainty Δ of respectively colored rpm case. Gray dashed lines indicate the lowest and upmost edges of EE impeller blades. (For interpretation of the references to color in this figure legend, the reader is referred to the web version of this article.)

3.2. Vertical probabilities of presence

Although the LSPs are adjusted close to a neutral buoyancy in the respective medium of use (Table 1), it is of essence to conduct an axial distribution assessment within the entire reactor to evaluate further results. In Fig. 13 (Appendix A), an exemplary axial movement sequence over approx. 1700 s of the LSP (ID 3) of trial no. 3 (LSP3-3) is depicted over the normalized reactor height together with a schematic view of the impeller blade positions. The LSP seems to flow primarily at the height of the impellers, whereas the lower and upper regions are less covered. A total time of at least 245 min is recorded with four LSPs for each rpm case. The resulting axial probability of presence for 15 (blue), 25 (green) and 40 rpm (red) is plotted in Fig. 4 with their respective uncertainties.

Despite their density adjustment for the respective reactor medium, the trend for 15 rpm reveals an accumulation with up to 4 % probability of presence at the reactor bottom, up to the lower dashed line, which indicates the lower edge of the first EE impeller stage. Beyond this point, which coincides with the location of the three EE impeller stages, the distribution becomes more uniform, resembling the trend of the 25 and 40 rpm case. Above the upper dashed line, which corresponds to the upper edge of the third EE impeller stage, all probabilities with exception to the 40 rpm case progressively decrease until lower than 1 % at the fluid's surface. Generally, the 40 rpm case is axially comparatively best distributed, however, showing a lack of data points at the bottom of the reactor. During the experiments at $T = 37\,^{\circ}\mathrm{C}$, it was found that

the density of the LSPs may decrease to a minimum of $(\rho_f - 1)\,\mathrm{kg\,m^{-3}}$ depending on their operating duration. It is assumed that the enclosed air, which is at room temperature when calibrating, equilibrates to the surrounding temperature in the medium, and thus leading to an increased pressure inside by a factor of approx. 1.05. As a result, the LSP's volume gradually increases by a theoretical amount of approx. $37 \cdot 10^{-9}\,\mathrm{m^3}$. The change of volume proves to be sufficient resulting in a density reduction of $\delta\rho_p \leq 1\,\mathrm{kg\,m^{-3}}$. Taking the hydrostatic pressure into consideration, this effect should be equalized below the normalized height of $z\,H^{-1} \approx 0.88$ depending on the stability of the LSP and its sealing components.

Due to the described sensitive density effect, the axial probability of presence over the reactor height is evaluated for the 35 rpm case for both medium types and quantitatively compared in Fig. 14 in Appendix B. It can be observed that the distributions in the center region are similar within their uncertainties for both medium types, in deionized water (DW) and in the isotonic solution (IS). Aside from that, both the bottom and upper region show a slightly increased divergence, respectively, up to 1 %.

3.3. Axial velocity distributions

Based on the flow direction of the LSPs, positive (upwards movement, solid lines) and negative (downwards movement, dashed lines) axial velocities are obtained by using the derivative of the vertical position concerning the recording frequency, which is depicted in Fig. 5.

By plotting three exemplary impeller frequencies as 15 (blue), 25 (green) and 40 rpm (red), an overall consistent pattern can be observed. In case of $|\overline{v}|_{z,\mathrm{neg}}$, two peaks occur at normalized reactor heights of $z\,H^{-1} \approx 0.20$ and 0.65. For 25 and 40 rpm, a third peak emerges at $z\,H^{-1} \approx 0.45$. A single peak is detectable for the trend of $\overline{v}_{z,\mathrm{pos}}$ at $z\,H^{-1} \approx 0.20$. This behavior can be attributed to the general pumping nature of a multi-stage axial-pumping agitator, whereby all heights match the center of any impeller stage, respectively. For all studied rpm cases, at $z\,H^{-1} \approx 0.65$, the LSPs reach their respective maximum downward flow velocity of $|\overline{v}|_{z,\mathrm{neg}} \in \{0.21, 0.37, 0.54\}\,\mathrm{m\,s^{-1}}$ due to a strong axial suction behavior of the third impeller stage. This behavior decreases slightly towards the vertical center of the reactor, then increases with higher impeller frequencies at the second stage, and finally increments to a last peak at $z\,H^{-1} \approx 0.20$. Here, they are pumped either into the less turbulent bottom region of the reactor, where their velocity is distinctively decreased, or are instantly redirected towards the reactor walls and baffles from where they move upwards. The latter is indicated by a single peak in all trends of upwards velocities with $\overline{v}_{z,\mathrm{pos}} \in \{0.18, 0.29, 0.49\}\,\mathrm{m\,s^{-1}}$, respectively. These velocities progressively decrease further, eventually falling below $0.1\,\mathrm{m\,s^{-1}}$ above the third impeller stage, which signifies a similar behavior to that observed in the bottom region. Hence, the fluid flow followed by the LPSs is mainly downwards in the proximity of the impellers and upwards near the reactor wall. The comparatively high uncertainty at 40 rpm for $z\,H^{-1} < 0.05$ is due to the sparse data points available for evaluation, as seen in Fig. 4.

As shown for the probability of presence, also the LSP's average axial velocity is scrutinized regarding both medium types, DW and IS, at two different temperatures, and depicted in Fig. 15 in Appendix C. Despite the previously described behavior as two peaks for $|\overline{v}|_{z,\mathrm{neg}}$ and one peak for $\overline{v}_{z,\mathrm{pos}}$ at the respective heights, only minor differences occur in the vertical center region of the reactor. However, especially in the reactor bottom region and at the center height of the third impeller stage, velocity differences of $\delta\overline{v}_{z,\mathrm{pos}} = 0.12\,\mathrm{m\,s^{-1}}$ and $\delta|\overline{v}|_{z,\mathrm{neg}} = 0.05\,\mathrm{m\,s^{-1}}$ are shown, respectively. Nevertheless, since for both medium types similar trends and values are shown, upcoming evaluations for all rpm cases are directly compared with each other independently of their media type.

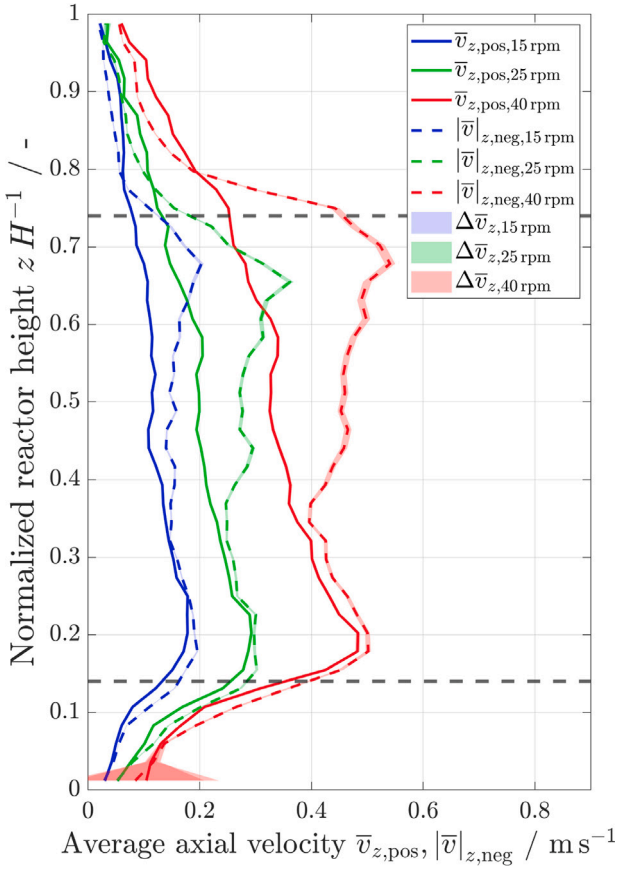

Fig. 5. Average positive (solid lines, upwards flow) and negative (dashed lines, downwards flow) axial velocity distributions over the normalized reactor height ($H = 4.2$ m) for four LSP data sets for each impeller frequency as 15 (blue), 25 (green) and 40 rpm (red) for a vertical bin size of 10 cm. Shaded areas show uncertainty Δ of respectively colored data set. Gray dashed lines indicate the lowest and upmost edges of EE impeller blades. (For interpretation of the references to color in this figure legend, the reader is referred to the web version of this article.)

3.4. Circulation time distributions

The circulation time $t_{\mathrm{circ},z}$ of an LSP is referred to the axially central plane of the reactor volume j at the height z and is determined by means of its passage time difference from top to bottom through that plane. Hence, this method yields a circulation time distribution (CTD) per height z.

An exemplary illustration of a CTD is shown in Fig. 6, for the 15 rpm case at a normalized reactor height of $z\,H^{-1} = 0.22$, which constitutes for the axial center of the first impeller stage. As previous studies have shown (Middleton, 1979; Bisgaard et al., 2021a; Mann et al., 1981; Reinecke, 2013), the CTD is log-normally distributed, as long as sufficient data points are obtained. In Fig. 6, a total of 441 single circulation time values are utilized, which are stacked above each other in a bar plot. As a reference, the mean value ($t = 34.9$ s, light gray dotted line), the median value ($t = 20.9$ s, gray dash-dotted line), and the weighted average value ($t = 35.2$ s, dark gray dashed line) are shown. However, due to a partly sparse availability of data points at the bottom and top of the reactor, large values may severely influence the average value, albeit not being necessarily representative. Consequently, presuming a distribution with at least 400 data points per bin as significant as shown in Fig. 6, for the normalized reactor height of e.g. $z\,H^{-1} = 0.86$, which is located in the center between the upper edge of the third impeller stage and the media surface, it would require a 10-fold longer recording time (approx. 11 h with four simultaneously used LSPs), owed to a total of 46 data points for the

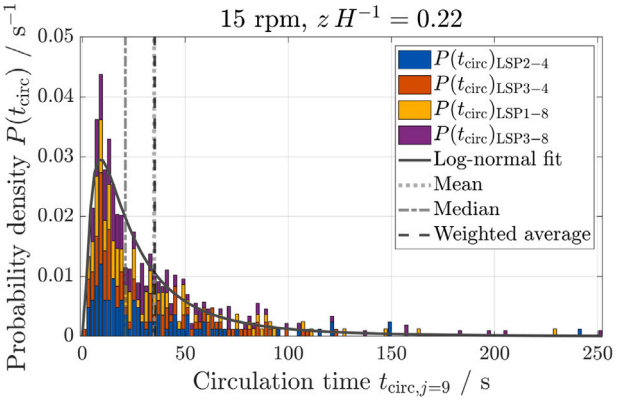

Fig. 6. Exemplary probability density $P(t_{circ})$ of the circulation time distribution for all four LSPs (ID 2 and ID 3 of experiment no. 4, ID 1 and ID 3 of experiment no. 8) at 15 rpm at a normalized reactor height of $z\,H^{-1} = 0.22$. A log-normal fit (black curve), the mean ($t = 34.9$ s, light gray dotted line), median ($t = 20.9$ s, gray dash-dotted line) and weighted average ($t = 35.2$ s, dark gray dashed line) are depicted based on 441 data points. (For interpretation of the references to color in this figure legend, the reader is referred to the web version of this article.)

respective bin. Due to differing recording lengths of the four utilized LSPs, the weighted average is chosen for representing $\bar{t}_{circ}$ for the corresponding reactor height z.

By plotting those weighted average values $\bar{t}_{circ,z}$ over the normalized reactor height in Fig. 7, an overall insight into the axial homogeneity of the macromixing process can be attained (Bajpai and Reuss, 1982). Moreover, one turn-over point is determined for each rpm case, which constitutes to the reactor height z of the shortest average circulation time as described by Reinecke (2013). For all impeller frequencies, this plane is between $0.19 < z\,H^{-1} < 0.24$, constituting the vertical center of the first impeller stage, with values of $\bar{t}_{circ,z} \in \{34.6, 22.2, 13.2\}$ s, for 15, 25 and 40 rpm, respectively. Notably, the circulation times exhibit a relatively shallow trend within this range, expanding over a centrally located regime between $0.15 \lesssim z\,H^{-1} \lesssim 0.75$. Beyond this, a strong increase in circulation times and their uncertainties mark both a top and a bottom regime with approx. 10-fold higher values. High uncertainties are attributed to the lack of data points in respective bins as previously described.

With the approach described in Section 2.7, quantitative regime zoning provides information about hydrodynamic compartments and their distinct boundaries, which are situated in the vicinity of the lower and upper edge of the first and third impeller stage, respectively (gray dashed lines). Furthermore, a respective average overall circulation time $\bar{t}_{circ,overall}$ can be calculated by means of the weighted average, which is (61.8 ± 2.8) s for 15 rpm, (38.2 ± 1.4) s for 25 rpm and (24.2 ± 0.7) s for 40 rpm (see Table 4).

3.5. Residence time distributions

Utilizing the calculation approach described in Section 2.6, average hydraulic residence time distributions (RTD) are presented in Fig. 8 for impeller frequencies as 15 (blue), 25 (green) and 40 rpm (red) over the normalized reactor height. Essentially, these values describe the average time of an LSP within a reactor volume V_j, based on its average velocity and consequently its direction as $|\bar{v}|_{j,down}$ or $\bar{v}_{j,up}$. This information further specifies whether the LSP is assumed to be located in the inner $V_{j,inner}$ or in the outer $V_{j,outer}$ reactor volume, respectively. Hence, the average inner $\bar{\tau}_{inner,z}$ and outer $\bar{\tau}_{outer,z}$ residence time is derived.

Similar to the trends shown in Fig. 7, three characteristic regimes are calculated for each impeller frequency: a center regime with comparatively low values at the height of the EE impeller stages, and a top

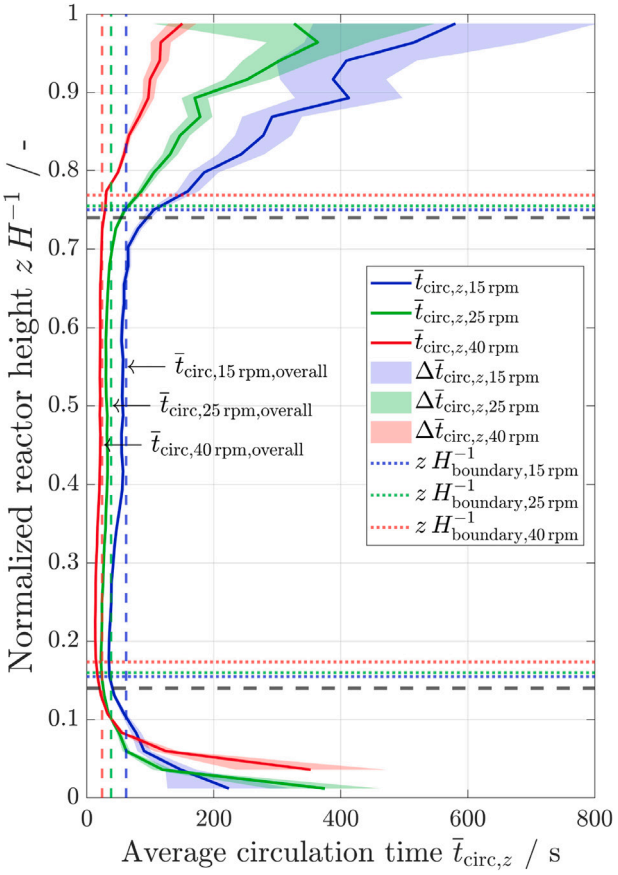

Fig. 7. Average circulation time distribution over the normalized reactor height ($H = 4.2$ m) for four LSP data sets for each impeller frequency of 15 (blue), 25 (green) and 40 rpm (red) for a vertical bin size of 10 cm. Shaded areas show uncertainty Δ, horizontal dotted lines show hydrodynamic compartment boundaries (see Section 2.7) and vertical dashed lines show the overall weighted average value of the respectively colored data set. Gray dashed lines indicate the lowest and upmost edges of EE impeller blades. (For interpretation of the references to color in this figure legend, the reader is referred to the web version of this article.)

and a bottom regime with higher values. Generally, in the vertical center and in the reactor bottom, residence times in the inner volume are lower than those in the outer volume, meaning a more rapid passage in the vicinity of the impellers or below than near the reactor wall. Nevertheless, between a normalized reactor height of $0.2 < z\,H^{-1} < 0.35$ both trends tend to approach similar values at $\bar{\tau} \in \{0.2, 0.4, 0.6\}$ s or cross each other so that $\bar{\tau}_{inner} > \bar{\tau}_{outer}$. Moreover, when comparing the latter observation with the average axial velocity distribution results in Fig. 5 at the same height, where also both upwards and downwards velocity values almost align, it can be deduced that in this region a comparatively high turbulence occurs. The underlying data regarding the calculated surface areas of the respective reactor volumes (not shown here) demonstrate for both upwards and downwards flows a similar area ($A_1 \approx A_2 \approx 0.5 \cdot A_{STR}$). Hence, most likely induced by the emerging stagnation pressure in the rather less turbulent bottom regime, the first impeller stage exhibits an increased radial pumping character. This effect could only be estimated if solely the data of the CTD were available, since the separation of the flows and resulting residence times could not be resolved. Yet, the CTD confirms the described effect by showing the lowest average circulation times in this region (Fig. 7). Furthermore, it can be observed that just above the third EE impeller stage, at $z\,H^{-1} \approx 0.75$, the respective trends of the inner and outer residence times cross and show $\bar{\tau}_{inner} > \bar{\tau}_{outer}$. Similarly to Fig. 5, where respective positive and negative velocity trends also cross at the height, the upper regime generally demonstrates high residence times

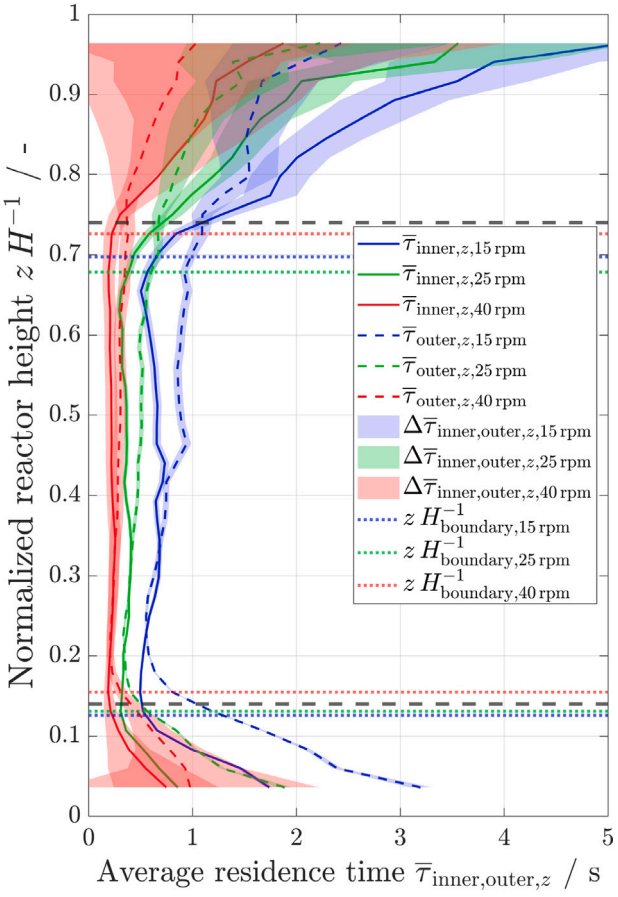

Fig. 8. Average hydraulic residence time distribution for both the inner $V_{j,\mathrm{inner}}$ and outer reactor volume $V_{j,\mathrm{outer}}$ over the normalized reactor height (H = 4.2 m) for four LSP data sets for each impeller frequency as 15 (blue), 25 (green) and 40 rpm (red) for a vertical bin size of 10 cm. Shaded areas show uncertainty Δ and horizontal dotted lines show hydrodynamic compartment boundaries (see Section 2.7) with respect to the inner residence time of the respectively colored data set. (For interpretation of the references to color in this figure legend, the reader is referred to the web version of this article.)

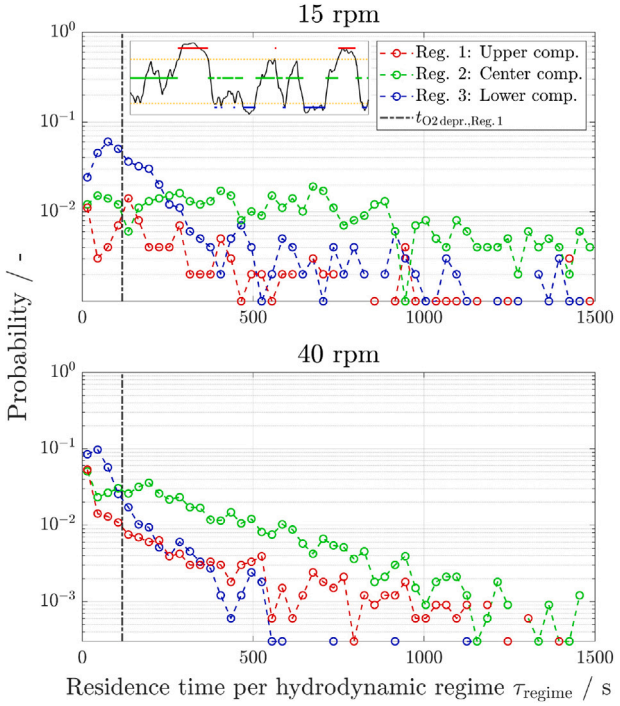

Fig. 9. Based on the calculated hydrodynamic compartment barriers resulting from the circulation time distribution (Fig. 7), residence time probability distributions per regime are shown for the upper (red), center (green) and lower compartment (blue) for both 15 and 40 rpm. The inset depicts the lifeline discretization with the respective color and the vertical dashed line an assumed temporal oxygen deprivation limit for a CHO cell cultivation in the upper compartment. (For interpretation of the references to color in this figure legend, the reader is referred to the web version of this article.)

with comparatively high uncertainties due to the lack of data points as described in previous sections. For further evaluations, these residence times are added up respectively in order to obtain the overall added hydraulic residence time (see Eq. (29)) and are stated in Table 4.

3.6. Lagrangian regime analysis

For the first time, LSP data provides emerging advancements with respect to an experimental, hydrodynamic Lagrangian regime analysis on industrial scale. This study does not focus on metabolic regimes, as demonstrated in Haringa et al. for an aerated yeast fermentation in a 22 m^3 fermentor (Haringa et al., 2017, 2018), but on single-phase hydrodynamic regimes. As described and depicted in Section 3.4, the compartment barriers are calculated based on the circulation time distribution and hereinafter utilized by discretizing the LSP's axial lifeline into three regimes. Fig. 9 depicts the residence time distribution (RTD) for the impeller frequencies 15 and 40 rpm per hydrodynamic regime τ_{regime} (upper (red), center (green) and lower (blue) compartment).

Intricate flow patterns emerge in shown compartments, specifically the RTD for 40 rpm demonstrates the characteristic exponential decay of a recirculation flow as already demonstrated by Haringa et al. (2018). They show a similar distribution behavior, although a comparatively dense amount of data from numerical simulations is used, in combination with a four-staged, six-bladed Rushton turbine (RT-6) agitator and the discretization into metabolic regimes with different specific substrate uptake rates (Haringa et al., 2018, 2017). Due to the comparatively large size of the center compartment in this study, for both rpm cases, the LSPs are more likely to stay in the center than in the lower or upper regime. Generally, the RTDs at 15 rpm are more equally distributed than for the 40 rpm case. This means a higher exchange rate for the latter, and thus the higher the impeller frequency the shorter the individual periods of residence times. When analyzing the total regime residence time percentage ratio, it becomes apparent that the LSPs only stay in the upper compartment 11.4 % and 17.6 % of the total recording time (≈ 264 min) in case of 15 and 40 rpm, respectively. The higher value for the latter may be attributed to the slight density shift during the experiments at T = 37 °C. It is to be noted that the upper compartment, however, makes up approx. 25 % of the total volume.

Furthermore, with the assumptions that LSPs mimic CHO cells during a cultivation, and that the aeration rate in the process does not influence the inherent measured hydrodynamic behavior, theoretical oxygen deprivation times in the upper compartment can be estimated. Hence, the proportion of cells inside the reactor, which are potentially exposed to oxygen deprivation conditions (Paul et al., 2004) can be ascertained. For a CHO cell cultivation, a maximum oxygen consumption rate is found to be approx. $0.6 \cdot 10^{-16}$ mol $cell^{-1}$ s^{-1} (Ihling et al., 2022). With a viable cell count of approx. $15 \cdot 10^6$ mL^{-1} (De Jesus and Wurm, 2011; Wurm, 2004) and the assumption of a zero-order kinetics, it would take ≈ 117 s (vertical dashed lines in Fig. 9) to reduce the dissolved oxygen from 60 % of air saturation to lower than 10 % at 37 °C ($K_{\mathrm{O2,H2O}}$ = 93.9 Pa m^3 mol^{-1}, $\xi^*_{\mathrm{O2,H2O}}$ = $6.8 \cdot 10^{-3}$ kg m^{-3}) (Paul et al., 2004). Concluding, 8.9 % and 8.4 % of the entire recording time, oxygen deprivation conditions are likely to occur for 15 and 40 rpm, respectively (see Table 4). A recent scale-down study (Wang et al., 2023) on *Penicillium chrysogenum* demonstrated a significant penicillin productivity reduction during dynamic starvation conditions (150 s)

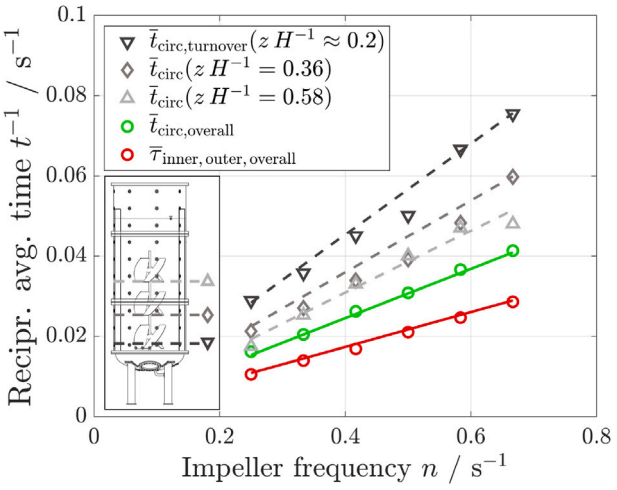

Fig. 10. Reciprocal average times of LSP measurement results (see Eq. (33)) as a function of the impeller frequency. Evaluated times are the average circulation times at three planes in the reactor ($z\,H^{-1} \in \{\approx 0.2, 0.36, 0.58\}$ - black, dark gray and light gray), respectively, the average overall circulation time (green) and the overall added hydraulic residence time (red). The slope k_{to} reveals the different Flow numbers. (For interpretation of the references to color in this figure legend, the reader is referred to the web version of this article.)

by a factor of two. Furthermore, Qian et al. (2014) described dissolved oxygen values of less than 15 % as hypoxic conditions for CHO cells, which results in a decrease of protein productivity. Moreover, Gaugler et al. (2023) conducted CHO cell cultivations in a single multi-compartment bioreactor (SMCB) as a scale-down model, mimicking large-scale mixing and found a reduction of the viable cell count in the stationary phase in combination with an increment of lactate concentration while the cells were exposed to enhanced oxygen gradients. Similar results are described by Anane et al. (2021) for dissolved oxygen gradients and by Gao et al. (2016) by means of fibronectin as a biomarker for hypoxic stress in a 5000 L bioreactor.

3.7. Flow number and mixing time correlations

Since most mixing experiments are conducted with six-bladed Rushton turbines (RT-6) and/or three-, four- or six-bladed pitched blade turbines (PBT-3, PBT-4, PBT-6), the latter displays a rough indication for herein calculated Flow number values for the EE impeller agitator, due to their common predominant axial pumping direction. To the best of the author's knowledge, no literature values are available for the EE impeller ABEC design. With the regression method described in Section 2.9, the different Flow numbers are scrutinized. As expected, Fig. 10 indicates an indirect proportionality between the plotted averaged times and the impeller frequency.

With the values shown in Table 3 it becomes apparent that the Flow number based on the average overall circulation time as $N_{\mathrm{Q,c,overall}} = 1.00$ seems not to be comparable to literature results, presumably due to the 3-staged design and especially the consideration of the upper compartment, where no active pumping takes place. Taking the ratio between the latter and $N_{\mathrm{Q,r}}$, it follows that $\bar{t}_{\mathrm{circ,overall}} = 0.71 \cdot \overline{\tau}_{\mathrm{overall}}$, which infers that the LSP's circulation on average covers the axial center region and does not close the loop often enough to cover the bottom and top region sufficiently. This time margin explains again the formation of the previously described compartments with their marked boundaries. In case of a multi-staged agitator, Schubert (2008) suggest that circulation numbers should be referred to one impeller each. Hence, after calculating those for the depicted positions (see Fig. 10), the average Circulation Flow number of $N_{\mathrm{Q,c,1}}$, $N_{\mathrm{Q,c,2}}$ and $N_{\mathrm{Q,c,3}}$ is $\overline{N}_{\mathrm{Q,c}} = 1.53 \pm 0.30$, which is in the range of literature results obtained by different LSPs in STRs, although single-staged PBTs with a lower Po in a reactor with $H\,d_{\mathrm{STR}}^{-1} \leq 1$ were used. Interestingly, $N_{\mathrm{Q,r}}$ is very similar to literature values stated as $N_{\mathrm{Q,p}}$. And furthermore, Schubert and Liepe's approach of $Q_{\mathrm{c}} \approx Q_{\mathrm{p}} \cdot \left(d_{\mathrm{STR}}\,d_{\mathrm{imp}}^{-1}\right)$ puts this study's results in a fitting ratio, if $N_{\mathrm{Q,p}} = N_{\mathrm{Q,r}}$ and $d_{\mathrm{STR}}\,d_{\mathrm{imp}}^{-1} = 2.19$ so that $\overline{N}_{\mathrm{Q,c}} \approx N_{\mathrm{Q,r}} \cdot 2.19 = 1.55$ (see Eqs. (30) and (31)).

Those estimations imply that although three impeller stages are installed in this study's reactor resulting in a $\mathrm{H}\,d_{\mathrm{STR}}^{-1}$ per impeller stage of 0.7, the overall pumping number is similar to a one-staged EE impeller with a much lower Po number without any compartment formation. Furthermore, the circulation time correlation of Middleton (Middleton, 1979), which is stated as

$$\bar{t}_{\mathrm{circ}} = 0.5 \cdot V^{0.30} \cdot \frac{1}{n}\left(\frac{d_{\mathrm{STR}}}{d_{\mathrm{imp}}}\right)^{3} \tag{35}$$

and was obtained with radio pills in multiple reactors ($H\,d_{\mathrm{STR}}^{-1} = 1$) with volumes up to 4.4 m^3, equipped with one Rushton turbine, underestimates the herein presented results by a factor of 2, albeit the overall added residence time instead of the average overall circulation time. The model described by Schubert and Liepe (Schubert, 2008) slightly overestimates this study's results by $\delta N_{\mathrm{Q,c}} \approx 0.38$, yet matches obtained $N_{\mathrm{Q,c,1}}$ for the turn-over point. In addition, Herbert et al. (1994) and Nienow (1996) describe the functionality $N_{\mathrm{Q,p}} \sim Po^{1/3}$, which would yield $N_{\mathrm{Q,p}} \in \{0.91, 1.06\}$ for $Po \in \{3.35, 5.3\}$ for a single-staged EE in a 3 L STR (not shown here, equal reactor ratios) and the three-staged EE in this study, respectively. Those values are slightly higher than those described by Simmons et al. (2007) and Zhu et al. (2009), who use, however, the Applikon design with a lower Power number. Moreover, the Exchange Flow numbers provide model parameters regarding the root mean square of the exchange flow rate at both the lower compartment boundary (at approx. $z\,H^{-1} = 0.15$) and the upper compartment boundary (at approx. $z\,H^{-1} = 0.75$). Results show in this single-phase flow double the exchange flow rate towards the lower regime than towards the upper regime.

In Fig. 11 (left) the results in terms of the relation between the average overall circulation times (green dots), average overall added residence times (red dots) and global mixing times (blue dots) against the volumetric power input are depicted. It can be observed that all three plotted times show a general asymptotic decreasing trend towards a respective characteristic value with an increasing $P\,V^{-1}$ ratio. Moreover, the global mixing time trend is congruent with the overall added residence times within their standard deviation or uncertainty. This is especially the case for higher specific power inputs. In case of lower volumetric power inputs, the mixing times are similar to those of the average overall circulation time within their standard deviation or uncertainty. The low standard deviations of the latter can be explained by taking the weighted average circulation time value at the reactor heights and considering their total number of counts.

Similar to the results in Bisgaard et al. (2021a), in Fig. 11 (right) a linear regression of both the average overall circulation time and the overall added residence time to the global mixing time is denoted. With a slope of 1.00±0.29 and 0.64±0.20, they show a comparatively high confidence bound for their fit, respectively. Especially the latter lies within a 15 % margin of the interpolated mixing times, however, they both could also be described by a sigmoidal trend. In contrast to literature statements, which indicate $3 \cdot t_{\mathrm{circ}} < t_{\mathrm{mix,global,95}} < 5 \cdot t_{\mathrm{circ}}$ (Nienow, 1996, 1998; Voncken et al., 1964; Khang and Levenspiel, 1976) based on conductivity measurements, however, with utilizing a single-staged RT-6 setup, Bisgaard et al. (2021a) found a relation of $t_{\mathrm{mix,global,95}} = 2.6 \cdot t_{\mathrm{circ}}$ with a single-staged PBT-4 and $t_{\mathrm{mix,global,95}} = 2.2 \cdot t_{\mathrm{circ}}$ with a single-staged RT-6 utilizing LSPs. They interpret their low values with the tracer detection position described in Holmes et al. (1964) at half of the liquid height, which therefore represents only "half a circulation" (Bisgaard et al., 2021a). This does not explain, however, the minor difference of only 0.4 between the RT-6 and PBT-4 impeller, although both clearly exhibit a different hydrodynamic flow pattern. Further comparing their

Table 3
Turn-over constants k_{to} according to Eq. (33), and Flow numbers according to Eqs. (30) and (34) (Pumping number $N_{Q,p}$, Circulation Flow number $N_{Q,c}$, Residence Flow number $N_{Q,r}$ and Exchange Flow number $N_{Q,e}$) with literature values and correlations. Respective slopes are depicted in Fig. 10. h_{Bm}: off-bottom clearance to first impeller stage; c_I: momentum flow number; rms: root mean square.

k_{to}/-	Flow number/-	Comments
–	$N_{Q,p} \sim Po^{1/3} \in \{0.91, 1.06\}$	Pitched Blade/Hydrofoils, with $Po \in \{3.35, 5.3\}$ (Nienow, 1996; Jaworski et al., 1996; Weetman and Oldshue, 1988)
–	$N_{Q,p} = 0.87$	1x up-pumping EE (Applikon), $Po \approx 1.7$, $d_{imp}\, d_{STR}^{-1} = 0.45$ (Simmons et al., 2007)
–	$N_{Q,p} = 0.73$	1x down-pumping EE (Applikon), $Po \approx 2.1$, $d_{imp}\, d_{STR}^{-1} = 0.45$ (Zhu et al., 2009)
–	$N_{Q,c} = 1.91$	Axial flow, $h_{Bm} = 0.65$ m, $c_I = 0.9$ (Schubert, 2008) (p. 1076)
0.13	$N_{Q,c} = 1.45$	LSP meas.: 1x down-pumping PBT-3, $Po \approx 1.2$, $d_{imp}\, d_{STR}^{-1} = 0.3$ (Reinecke, 2013)
–	$N_{Q,c} = 1.39$	LSP meas.: 1x down-pumping PBT-4, $d_{imp}\, d_{STR}^{-1} = 0.32$ (Bisgaard et al., 2021a)
0.06	$N_{Q,c,overall} = 1.00$	this study, avg. overall circulation time
0.11	$N_{Q,c,1} = 1.85$	this study, avg. circulation time at $z\, H^{-1} \approx 0.2$ (turn-over point)
0.09	$N_{Q,c,2} = 1.47$	this study, avg. circulation time at $z\, H^{-1} = 0.36$
0.08	$N_{Q,c,3} = 1.26$	this study, avg. circulation time at $z\, H^{-1} = 0.58$
0.04	$N_{Q,r} = 0.71$	this study, overall added inner and outer residence times
–	$N_{Q,e,low} = 1.31 \pm 0.07$	this study, rms of inner and outer volume flow at $z\, H^{-1} = 0.15$
–	$N_{Q,e,up} = 0.62 \pm 0.08$	this study, rms of inner and outer volume flow at $z\, H^{-1} = 0.75$

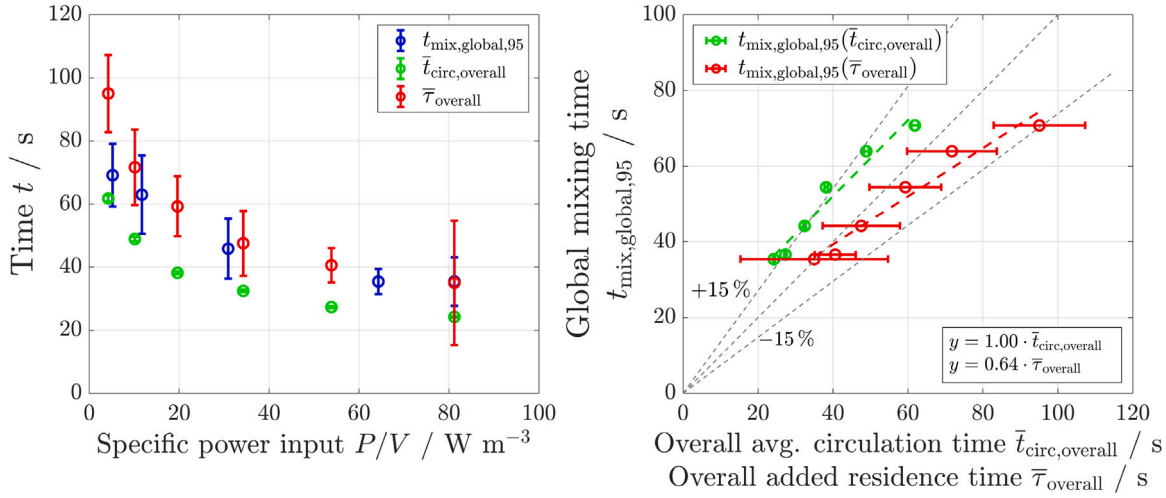

Fig. 11. Measured global mixing time (blue dots), average overall circulation time (green dots) and overall added hydraulic residence time (red dots) as a function of the specific power input (left) and the last two as a function of extrapolated global mixing times according to measured values with a respective linear regression (right). (For interpretation of the references to color in this figure legend, the reader is referred to the web version of this article.)

results to this study's results quantitatively, concludes to the possibility that either their pH probe measured excessive mixing times due to a long response time or low circulation times due to an insufficient flow-following behavior in a comparatively small tank and a similar LSP size. Moreover, a model approach by van de Vusse (1962) considering up to four mixing stages assumes a complete homogenization of the tank after about one circulation, which would fit this study's result. Nevertheless, all contemplate a one-staged agitator with a $H\, d_{STR}^{-1} = 1$ ratio.

Additionally, for a comparison in a dimensionless way, obtained times can be multiplied with respective impeller frequencies and plotted as a function of the stirrer Reynolds number (Zlokarnik, 2001; Rosseburg et al., 2018), as seen in Fig. 12.

Correlating those to literature results should be treated with caution due to different $H\, d_{STR}^{-1}$ ratios (mostly = 1), single-staged agitators and especially mostly utilized RT-6 or PBT impellers on much smaller scales. Relevant mixing time correlations, which include the Circulation Flow number (Nienow, 1998) ($H\, d_{STR}^{-1} = 1$, RT-6, assumption that system is homogenized after five circulations),

$$t_{mix,Nie} \cdot n = 3.9 \cdot \left(\frac{d_{imp}}{d_{STR}}\right)^{-3} \cdot N_{Q,c}, \tag{36}$$

or the number of impellers i_{imp} (Vasconcelos et al., 1995) (1x RT-6 per $H\, d_{STR}^{-1} = 1$),

$$t_{mix,Vas} \cdot n = 2.3 \cdot \exp\left(0.68 \cdot \frac{d_{STR}}{d_{imp}} + 0.83 \cdot i_{imp}\right), \tag{37}$$

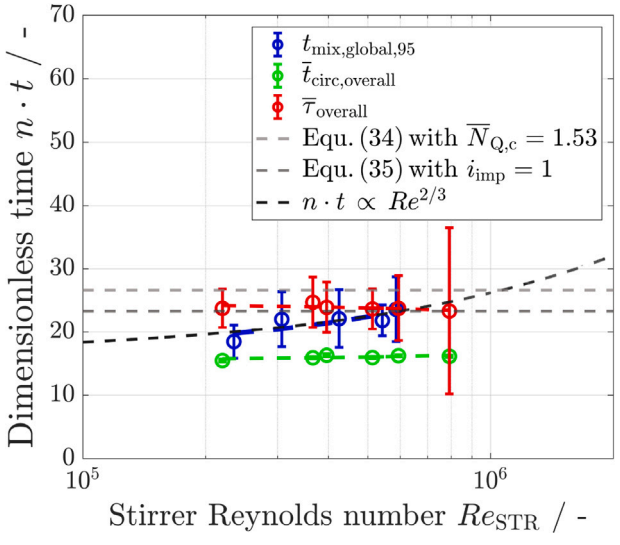

Fig. 12. Dimensionless global mixing time (blue dots), average overall circulation time (green dots) and overall added hydraulic residence time in dependency of the stirrer Reynolds number. Comparison between literature correlations and experimental results. (For interpretation of the references to color in this figure legend, the reader is referred to the web version of this article.)

Table 4
Overview of results of different St numbers, average overall circulation times, overall added residence times, respective correlated global mixing times, and percentages of theoretical O_2 deprivation conditions in the upper compartment.

	Stirring frequency n/ rpm					
	15	20	25	30	35	40
St in DW (based on resp. Taylor scale L_E)/–	4.0	4.7	5.1	5.4	5.7	6.2
St in IS (based on resp. Taylor scale L_E)/–	4.5	5.3	5.9	6.2	6.6	7.2
St (meso-scale)/–			0.17<St<0.18			
St (macro-scale)/–			≈ 0.004			
$\bar{t}_{circ,overall}$/s	61.8	48.9	38.2	32.4	27.3	24.2
$\Delta\bar{t}_{circ,overall}$/s	0.9	0.7	0.4	0.4	0.3	0.2
$\bar{\tau}_{overall}$/s	95.1	71.7	59.3	47.5	40.6	35.0
$\Delta\bar{\tau}_{overall}$/s	12.2	12.0	9.6	10.3	5.5	19.7
Correlated $t_{mix,global,95}$/s	70.8	64.0	54.5	44.2	36.6	35.4
Percentage of time in the upper compartment under theoretical O_2 deprivation conditions/%	8.9	9.3	8.3	11.3	6.9	8.4

anticipate a constant value when operating within the turbulent regime $Re_{STR} > 10^4$ and are overestimated by an approximate factor of 2 (if $N_{Q,c} = 1.0$) and 5.3 (if $i_{impeller} = 3$). Interestingly, the first shows a reasonable value if $\overline{N}_{Q,c} = 1.53$ is used ($t_{mix,Nie} = 26.6$ s) and the second, if $i_{imp} = 1$ ($t_{mix,Vas} = 23.3$ s), albeit herein measured results are clearly increasing with an increasing stirrer Reynolds number as already demonstrated in a previous study by Rosseburg et al. (2018). Generally, the trend of the global mixing time follows $n \cdot t \propto Re^{2/3}$, which is very similar as described by Zlokarnik ($n{\cdot}t \propto Re^{0.7}$) for a single-staged propeller if $Re_{STR} > 10^4$ (Zlokarnik, 1967). The correlation provided by Khang and Levenspiel (Khang and Levenspiel, 1976) by means of the decay rate constant K for propeller mixers (if $Re \geq 10^4$) is found to be $(n K^{-1})\left(d_{imp}\, d_{STR}^{-1}\right)^2 = 8.9 \pm 5.5$, which is overestimated by a factor of 10 and proportional to the increase of Po. As reported by Holmes et al. (1964), in terms of both the average overall circulation time and overall added residence time, they approach constant values, which are in this study 15.5 ± 0.8 and 24.5 ± 1.4, respectively. In light of utilizing a three-staged axially pumping EE impeller agitator with a $H\, d_{STR}^{-1} = 2.1$, their plotting approach could be extended so that $n \cdot \bar{t}_{circ,overall} \cdot \left(d_{imp}\, d_{STR}^{-1}\right)^2 \cdot d_{STR} \cdot (H\, n_{imp})^{-1}$, which would yield 0.51 and being approximately half of the value achieved by Holmes et al. with a single-staged RT-6 and a $H\, d_{STR}^{-1} = 1$ (Vrábel et al., 2000; Sieblist et al., 2011).

4. Conclusion

In this study, Lagrangian Sensor Particles (LSPs) with a macro-scale Stokes number $St \approx 0.004$, equipped with a pressure sensor, are utilized to investigate lifelines of cells in a 15,000 L stirred tank reactor (STR) with three Elephant Ear (EE) impellers. To hydrodynamically characterize the entire STR and analyze single-phase mixing heterogeneities within the bioreactor in form of compartments, the vertical probability of presence of the LSPs, axial velocity profiles, axial circulation time distributions and residence time distributions are quantified. The culmination of this is a Lagrangian regime analysis. Results are compared to experimentally determined global mixing times for the same setup and literature results from similar bioreactors of different scales.

For the examined operating points, the vertical probability of presence is similarly distributed throughout the vertical reactor center, however, decreases in the top and bottom of the STR. Solely in the case of the operating point with $n = 15$ rpm, the LSPs show a higher probability of presence towards the bottom of the reactor, emphasizing the sensitivity of the LSP to fluctuating densities. The characteristic down-pumping behavior of the EE impellers is depicted by the axial velocity distributions for both downwards and upwards flow. Peaks are evident for the upper impeller stage regarding the downwards flow (suction zone) and at the lowest impeller stage regarding the upwards flow (redirection zone).

By investigating the axial circulation time distributions (CTDs) over the reactor height, defined as the time between to consecutive LSP passages over a certain axial height, the resulting profile reveals distinctively shorter circulation times in the axial center region than in the regions below and above. In the last two, comparatively high uncertainties lead to the conclusion that a 10-fold longer measurement time is necessary to show a significant statistic for CTDs in the reactor bottom and top region. Nonetheless, for all operating points, three compartments are discerned, with an average overall circulation time being calculated.

With the assumption of a predominantly axial flow profile, the hydraulic residence time distribution (RTD) over the reactor height is calculated by introducing a model based on gained axial velocities. Inner and outer residence times reveal a similar profile as the previously derived CTDs with three compartments.

Consequently, a Lagrangian regime analysis is conducted based on the compartmentalization of the CTD data with a discretization of the LSP lifelines. These single-phase flow results allude to a potential oxygen deprivation zone for CHO cells in the upper compartment of at least 7 % of the experimental time, if similar hydrodynamics during a fermentation are assumed.

Furthermore, under the consideration of previous results, different Flow number calculations demonstrate that LSPs can be utilized to characterize impeller systems, and provide model parameters. Although literature values for a three-staged EE impeller system on industrial scale are not available, presented results are comparable.

Contrary to literature stating that the ratio of the global mixing time to circulation time falls between 2.2 and 5.0, this study, admittedly using a different impeller setup, reveals that both values exhibit no such dependency and instead maintain a ratio of 1.0. With the exception for $n = 15$ rpm, overall added residence time values are similar to the global mixing time, while within the respective uncertainty or standard deviation. Results highlight, that all three presented methods describe mixing on a macro-scale, for which the LSPs show a sufficiently small Stokes number.

This study demonstrates that LSP technology serves as an effective tool for investigating large-scale stirred tank reactors. Results showcase the capability of an LSP to detect hydrodynamic compartments, while not requiring optical access. To comprehensively determine the fluid flow, it is essential to further advance the LSPs through sensors making their localization possible, as they are currently limited to axial resolution. To better represent a cell within a bioreactor through an LSP and discern the respective process conditions experienced by a cell over the course of its lifeline, sensors for process parameters such as temperature, pH, dissolved oxygen and conductivity will be installed in the near future. Moreover, further development is necessary regarding their balancing, meaning the influence the position of the respective center of mass has on an LSP for more accurate results in detecting meso-scales and vortices. For smaller reactor scales, miniaturization proves highly advantageous, however, as this study shows, in

order to determine compartments on a macro-scale the flow-following capability of available LSPs proves to be sufficient.

CRediT authorship contribution statement

Sebastian Hofmann: Conceptualization, Methodology, Project administration, Software, Writing – original draft, Writing – review & editing, Supervision, Validation, Visualization, Data curation, Formal analysis, Investigation. **Lukas Buntkiel:** Conceptualization, Data curation, Formal analysis, Investigation, Methodology, Resources, Software, Validation, Visualization, Writing – original draft, Writing – review & editing. **Ryan Rautenbach:** Validation, Writing – review & editing, Conceptualization, Formal analysis, Investigation. **Lena Gaugler:** Conceptualization, Formal analysis, Investigation, Validation, Writing – original draft. **Yifan Ma:** Software, Conceptualization, Methodology, Resources. **Ingrid Haase:** Investigation, Methodology, Conceptualization, Data curation. **Jürgen Fitschen:** Investigation, Methodology, Data curation. **Thomas Wucherpfennig:** Funding acquisition, Resources, Supervision. **Sebastian Felix Reinecke:** Funding acquisition, Methodology, Supervision. **Marko Hoffmann:** Funding acquisition, Project administration, Resources, Writing – review & editing. **Ralf Takors:** Funding acquisition, Project administration, Resources, Supervision. **Uwe Hampel:** Funding acquisition, Resources, Supervision. **Michael Schlüter:** Conceptualization, Formal analysis, Funding acquisition, Supervision, Writing – review & editing.

Declaration of competing interest

The authors declare that they have no known competing financial interests or personal relationships that could have appeared to influence the work reported in this paper.

Data and code availability

Utilized MATLAB® scripts that were developed in order to evaluate the data can be publicly accessed at our Gitlab project. Raw data and results are publicly accessible in our DaRUS repository. Please contact Sebastian Hofmann or Lukas Buntkiel for further information.

Acknowledgments

The authors gratefully acknowledge the funding by the German Research Foundation (Deutsche Forschungsgemeinschaft - DFG) within the Priority Program SPP 2170 “InterZell” (Grant Number: 42789983). Parts of the HZDR’s work have been funded by the BMEL, Germany in the project SensOMix (FKZ 2219NR390), the project Neobio (FKZ 22032618), and from the Impulse and Networking fund of the Helmholtz Association, Germany within the framework of the Clean Water Technology Lab - A Helmholtz Innovation Lab (HIL-A02). In particular we would like to thank Marc Maly for proof-reading, and Jakob Schulze and Helena Ostrinsky for support during the experiments.

Appendix A. Exemplary axial movement of an LSP

See Fig. 13.

Appendix B. Axial probability of presence at 35 rpm

See Fig. 14.

Appendix C. Axial velocity distributions at 35 rpm

See Fig. 15.

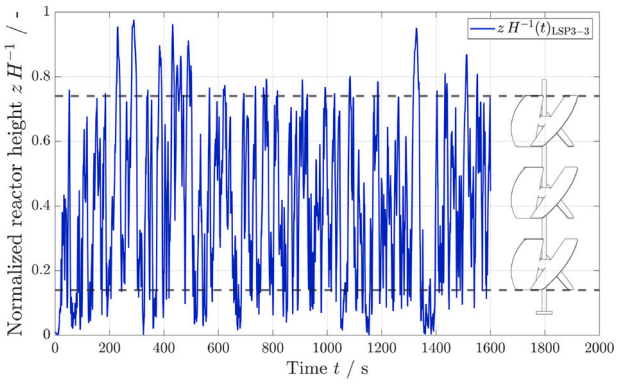

Fig. 13. Exemplary axial movement of the LSP (ID 3) of trial no. 3 (LSP3-3) at an impeller frequency of $n = 35$ rpm over time with indicated position of the Elephant Ear (EE) impellers and respective upper and lower edge (gray dashed lines).

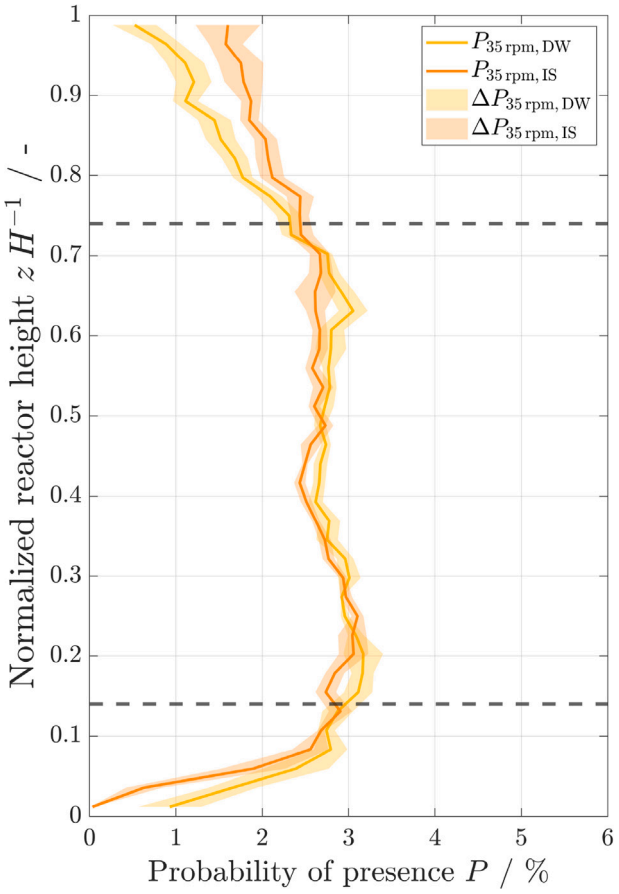

Fig. 14. Axial probability of presence over the normalized reactor height ($H = 4.2$ m) for four LSP data sets for each trend at 35 rpm in DW at $T = 20\,^{\circ}$C (yellow line) and in IS at $T = 37\,^{\circ}$C (orange line) for a vertical bin size of 10 cm. Shaded areas show uncertainty Δ of respective trend. Dashed lines indicate the lower and upper edge of EE impellers. (For interpretation of the references to color in this figure legend, the reader is referred to the web version of this article.)

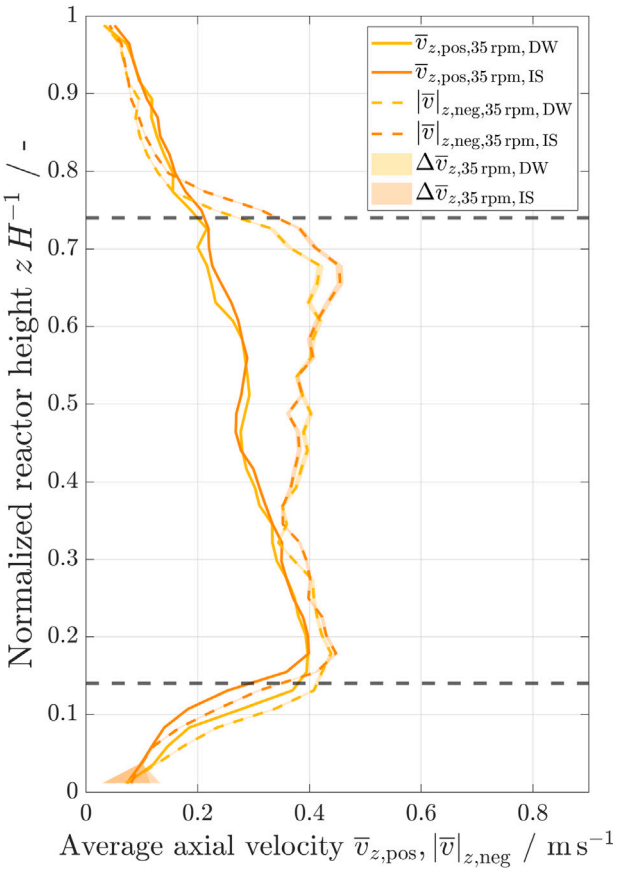

Fig. 15. Average positive (solid lines, upwards flow) and negative (dashed lines, downwards flow) axial velocity distributions over the normalized reactor height ($H = 4.2$ m) for four LSP data sets for each trend at 35 rpm in DW at $T = 20$ °C (yellow line) and in IS at $T = 37$ °C (orange line) for a vertical bin size of 10 cm. Shaded areas show uncertainty Δ of respectively colored data set. Dashed lines indicate the lower and upper edge of EE impellers. (For interpretation of the references to color in this figure legend, the reader is referred to the web version of this article.)

References

Anane, E., Knudsen, I.M., Wilson, G.C., 2021. Scale-down cultivation in mammalian cell bioreactors—the effect of bioreactor mixing time on the response of CHO cells to dissolved oxygen gradients. Biochem. Eng. J. 166, 107870. http://dx.doi.org/10.1016/j.bej.2020.107870.

Bajpai, R.K., Reuss, M., 1982. Coupling of mixing and microbial kinetics for evaluating the performance of bioreactors. Can. J. Chem. Eng. 60 (3), 384–392. http://dx.doi.org/10.1002/cjce.5450600308.

Bisgaard, J., Muldbak, M., Cornelissen, S., Tajsoleiman, T., Huusom, J.K., Rasmussen, T., Gernaey, K.V., 2020. Flow-following sensor devices: A tool for bridging data and model predictions in large-scale fermentations. Comput. Struct. Biotechnol. J. 18, 2908–2919. http://dx.doi.org/10.1016/j.csbj.2020.10.004.

Bisgaard, J., Muldbak, M., Tajsoleiman, T., Rydal, T., Rasmussen, T., Huusom, J.K., Gernaey, K.V., 2021a. Characterization of mixing performance in bioreactors using flow-following sensor devices. Chem. Eng. Res. Des. 174, 471–485. http://dx.doi.org/10.1016/j.cherd.2021.08.008.

Bisgaard, J., Tajsoleiman, T., Muldbak, M., Rydal, T., Rasmussen, T., Huusom, J.K., Gernaey, K.V., 2021b. Automated compartment model development based on data from flow-following sensor devices. Processes 9 (9), 1651. http://dx.doi.org/10.3390/pr9091651.

Blöbaum, L., Haringa, C., Grünberger, A., 2023. Microbial lifelines in bioprocesses: from concept to application. Biotechnol. Adv. 62, 108071. http://dx.doi.org/10.1016/j.biotechadv.2022.108071.

Bryant, J., Sadeghzadeh, S., 1979. Circulation rates in stirred and aerated tanks. In: Proceedings of the 3rd European Conference on Mixing: Held At the University of York, vol. 1, BHRA Fluid Engineering, Cranfield, Bedford, England, pp. 325–336.

Buntkiel, L., Ma, Y., Reinecke, S.F., Hampel, U., 2023a. Orientation resolved measurements of accelerations with sensor particles in bioreactors. tm - Tech. Mess. 90 (12), 835–845. http://dx.doi.org/10.1515/teme-2023-0115.

Buntkiel, L., Reinecke, S.F., Hampel, U., 2023b. Beschleunigungsmessung als Grundlage für die Strömungsverfolgung in Bioreaktoren mit Sensorpartikeln: Acceleration measurement for flow tracking in bioreactors with sensor particles. tm - Tech. Mess. 90 (s1), 43–48. http://dx.doi.org/10.1515/teme-2023-0078.

Collignon, M.-L., Delafosse, A., Crine, M., Toye, D., 2010a. Axial impeller selection for anchorage dependent animal cell culture in stirred bioreactors: methodology based on the impeller comparison at just-suspended speed of rotation. Chem. Eng. Sci. 65 (22), 5929–5941. http://dx.doi.org/10.1016/j.ces.2010.08.027.

Collignon, M.-L., Dossin, D., Delafosse, A., Crine, M., Toye, D., 2010b. Quality of mixing in a stirred bioreactor used for animal cells culture: Heterogeneities in a lab scale bioreactor and evolution of mixing time with scale up. BASE http://popups.ulg.be/1780-4507/index.php?id=6292&lang=en.

Crowe, C.T., Schwarzkopf, J.D., Sommerfeld, M., Tsuji, Y., 2011. Multiphase Flows with Droplets and Particles, second ed. CRC Press, http://dx.doi.org/10.1201/b11103.

Day, A.M., 1975. Mixing in Stirred Tanks (Ph.D. thesis). University of Exeter, University of Exeter.

De Jesus, M., Wurm, F.M., 2011. Manufacturing recombinant proteins in kg-ton quantities using animal cells in bioreactors. Eur. J. Pharmaceut. Biopharmaceut. 78 (2), 184–188. http://dx.doi.org/10.1016/j.ejpb.2011.01.005.

Delafosse, A., Collignon, M.-L., Calvo, S., Delvigne, F., Crine, M., Thonart, P., Toye, D., 2014. CFD-based compartment model for description of mixing in bioreactors. Chem. Eng. Sci. 106, 76–85. http://dx.doi.org/10.1016/j.ces.2013.11.033.

Delbridge, J.N., Barrett, T.A., Ducci, A., Micheletti, M., 2023. Power, mixing and flow dynamics of the novel Allegro™ stirred tank reactor. Chem. Eng. Sci. 271, 118545. http://dx.doi.org/10.1016/j.ces.2023.118545.

Enfors, S.-O., Jahic, M., Rozkov, A., Xu, B., Hecker, M., Jürgen, B., Krüger, E., Schweder, T., Hamer, G., O'Beirne, D., Noisommit-Rizzi, N., Reuss, M., Boone, L., Hewitt, C., McFarlane, C., Nienow, A., Kovacs, T., Trägårdh, C., Fuchs, L., Revstedt, J., Friberg, P., Hjertager, B., Blomsten, G., Skogman, H., Hjort, S., Hoeks, F., Lin, H.-Y., Neubauer, P., van der Lans, R., Luyben, K., Vrabel, P., Manelius, Å., 2001. Physiological responses to mixing in large scale bioreactors. J. Biotechnol. 85 (2), 175–185. http://dx.doi.org/10.1016/S0168-1656(00)00365-5.

Fitschen, J., 2021. Hydrodynamic Characterization of Heterogeneities in Aerated Stirred Tank Reactors - From an Eulerian to a Lagrangian Perspective (Ph.D. thesis). Hamburg University of Technology, Institute of Multiphase Flows.

Fitschen, J., Hofmann, S., Bernemann, V., 2021a. Gitlab repository: determination of local mixing time distribution in STR. https://collaborating.tuhh.de/v5/multiphase-bioreactors/sebastian-hofmann/determination-of-local-mixing-time-distribution-in-str,

Fitschen, J., Hofmann, S., Kursula, L., Haase, I., Wucherpfennig, T., Schlüter, M., 2023. Advances in characterization of industrial bioreactors for cell culture process. Biopharm. Manuf.: Prog., Trends Chall., : Cell Eng. 11, 67–111. http://dx.doi.org/10.1007/978-3-031-45669-5_3.

Fitschen, J., Hofmann, S., Wutz, J., Kameke, A., Hoffmann, M., Wucherpfennig, T., Schlüter, M., 2021b. Novel evaluation method to determine the local mixing time distribution in stirred tank reactors. Chem. Eng. Sci.: X 10, 100098. http://dx.doi.org/10.1016/j.cesx.2021.100098.

Gao, Y., Ray, S., Dai, S., Ivanov, A.R., Abu-Absi, N.R., Lewis, A.M., Huang, Z., Xing, Z., Borys, M.C., Li, Z.J., Karger, B.L., 2016. Combined metabolomics and proteomics reveals hypoxia as a cause of lower productivity on scale-up to a 5000-liter CHO bioprocess. Biotechnol. J. 11 (9), 1190–1200. http://dx.doi.org/10.1002/biot.201600030.

Gargalo, C.L., Udugama, I., Pontius, K., Lopez, P.C., Nielsen, R.F., Hasanzadeh, A., Mansouri, S.S., Bayer, C., Junicke, H., Gernaey, K.V., 2020. Towards smart biomanufacturing: A perspective on recent developments in industrial measurement and monitoring technologies for bio-based production processes. J. Ind. Microbiol. Biotechnol. 47 (11), 947–964. http://dx.doi.org/10.1007/s10295-020-02308-1.

Gaugler, L., Hofmann, S., Schlüter, M., Takors, R., 2023. Mimicking CHO large-scale effects in the single multicompartment bioreactor: A new approach to access scale-up behavior. Biotechnol. Bioeng. http://dx.doi.org/10.1002/bit.28647.

Gaugler, L., Mast, Y., Fitschen, J., Hofmann, S., Schlüter, M., Takors, R., 2022. Scaling-down biopharmaceutical production processes via a single multi-compartment bioreactor (SMCB). Eng. Life Sci. http://dx.doi.org/10.1002/elsc.202100161, elsc.202100161.

George, S., Larsson, G., Olsson, K., Enfors, S.-O., 1998. Comparison of the Baker's yeast process performance in laboratory and production scale. Bioprocess Eng. 18 (2), 135–142. http://dx.doi.org/10.1007/PL00008979.

Haider, A., Levenspiel, O., 1989. Drag coefficient and terminal velocity of spherical and nonspherical particles. Powder Technol. 58 (1), 63–70. http://dx.doi.org/10.1016/0032-5910(89)80008-7.

Haringa, C., 2023. An analysis of organism lifelines in an industrial bioreactor using Lattice-Boltzmann CFD. Eng. Life Sci. 23 (1), http://dx.doi.org/10.1002/elsc.202100159.

Haringa, C., Deshmukh, A.T., Mudde, R.F., Noorman, H.J., 2017. Euler-Lagrange analysis towards representative down-scaling of a 22 m 3 Aerobic s. Cerevisiae fermentation. Chem. Eng. Sci. 170, 653–669. http://dx.doi.org/10.1016/j.ces.2017.01.014.

Haringa, C., Mudde, R.F., Noorman, H.J., 2018. From industrial fermentor to CFD-guided downscaling: What have we learned? Biochem. Eng. J. 140, 57–71. http://dx.doi.org/10.1016/j.bej.2018.09.001.

Haringa, C., Tang, W., Deshmukh, A.T., Xia, J., Reuss, M., Heijnen, J.J., Mudde, R.F., Noorman, H.J., 2016. Euler-Lagrange computational fluid dynamics for (bio)reactor scale down: An analysis of organism lifelines. Eng. Life Sci. 16 (7), 652–663. http://dx.doi.org/10.1002/elsc.201600061.

Heins, A.-L., Lencastre Fernandes, R., Gernaey, K.V., Lantz, A.E., 2015. Experimental and in silico investigation of population heterogeneity in continuous sachharomyces cerevisiae scale-down fermentation in a two-compartment setup. J. Chem. Technol. Biotechnol. 90 (2), 324–340. http://dx.doi.org/10.1002/jctb.4532.

Herbert, R.-M., Knobling, K., Post, T., 1994. Mischzeitbestimmung schnell berechnet. Chem. Tech. 23, 40–41.

Herzog, J., Mook, A., Guhl, L., Bäumler, M., Beck, M.H., Weuster-Botz, D., Bengelsdorf, F.R., Zeng, A.-P., 2023. Novel synthetic co-culture of acetobacterium woodii and clostridium drakei using CO2 and in situ generated H2 for the production of caproic acid via lactic acid. Eng. Life Sci. 23 (1), e2100169. http://dx.doi.org/10.1002/elsc.202100169.

Ho, P., Täuber, S., Stute, B., Grünberger, A., von Lieres, E., 2022. Microfluidic reproduction of dynamic bioreactor environment based on computational lifelines. Front. Chem. Eng. 4, 826485. http://dx.doi.org/10.3389/fceng.2022.826485.

Ho, P., Westerwalbesloh, C., Kaganovitch, E., Grünberger, A., Neubauer, P., Kohlheyer, D., von Lieres, E., 2019. Reproduction of large-scale bioreactor conditions on microfluidic chips. Microorganisms 7 (4), 105. http://dx.doi.org/10.3390/microorganisms7040105.

Hoang, M.D., Doan, D.T., Schmidt, M., Kranz, H., Kremling, A., Heins, A.-L., 2022. Application of an Escherichia coli triple reporter strain for at-line monitoring of single-cell physiology during L-phenylalanine production. Eng. Life Sci. 23 (1), 15. http://dx.doi.org/10.1002/elsc.202100162.

Hofmann, S., Buntkiel, L., Rautenbach, R., Brouwers, I.S., 2023. Gitlab repository: ChERD data for LSP lifeline analysis. https://collaborating.tuhh.de/v5/multiphase-bioreactors/sebastian-hofmann/cherd-data-for-lsp-lifeline-analysis,

Hofmann, S., Weiland, C., Fitschen, J., von Kameke, A., Hoffmann, M., Schlüter, M., 2022. Lagrangian sensors in a stirred tank reactor: comparing trajectories from 4D-particle tracking velocimetry and lattice-Boltzmann simulations. 137549, Chem. Eng. J. 137549, 449, 22.http://dx.doi.org/10.1016/j.cej.2022.137549,

Holmes, D., Voncken, R., Dekker, J., 1964. Fluid flow in turbine-stirred, baffled tanks—I. Chem. Eng. Sci. 19 (3), 201–208. http://dx.doi.org/10.1016/0009-2509(64)85030-2.

Huilier, D.G.F., 2021. An overview of the Lagrangian dispersion modeling of heavy particles in homogeneous isotropic turbulence and considerations on related LES simulations. Fluids 6 (4), 145. http://dx.doi.org/10.3390/fluids6040145.

Ihling, N., Munkler, L.P., Paul, R., Berg, C., Reichenbächer, B., Kadisch, M., Lang, D., Büchs, J., 2022. Non-invasive and time-resolved measurement of the respiration activity of Chinese hamster ovary cells enables prediction of key culture parameters in shake flasks. Biotechnol. J. 17 (8), 2100677. http://dx.doi.org/10.1002/biot.202100677.

Jaworski, Z., Nienow, A.W., Dyster, K.N., 1996. An LDA study of the turbulent flow field in a baffled vessel agitated by an axial, down-pumping hydrofoil impeller. Can. J. Chem. Eng. 74 (1), 3–15. http://dx.doi.org/10.1002/cjce.5450740103.

Khang, S.J., Levenspiel, O., 1976. New scale-up and design method for stirrer agitated batch mixing vessels. Chem. Eng. Sci. 31 (7), 569–577. http://dx.doi.org/10.1016/0009-2509(76)80020-6.

Kratzl, F., Kremling, A., Pflüger-Grau, K., 2023. Streamlining of a synthetic co-culture towards an individually controllable one-pot process for polyhydroxyalkanoate production from light and CO2. Eng. Life Sci. 23 (1), e2100156. http://dx.doi.org/10.1002/elsc.202100156.

Kuschel, M., Fitschen, J., Hoffmann, M., von Kameke, A., Schlüter, M., Wucherpfennig, T., 2021. Validation of novel lattice Boltzmann large eddy simulations (lb LES) for equipment characterization in biopharma. Processes 9 (6), 950. http://dx.doi.org/10.3390/pr9060950.

Kuschel, M., Takors, R., 2020. Simulated oxygen and glucose gradients as a prerequisite for predicting industrial scale performance *a Priori*. Biotechnol. Bioeng. 117 (9), 2760–2770. http://dx.doi.org/10.1002/bit.27457.

Lapin, A., Müller, D., Reuss, M., 2004. Dynamic behavior of microbial populations in stirred bioreactors simulated with Euler-Lagrange methods: traveling along the lifelines of single cells. Ind. Eng. Chem. Res. 43 (16), 4647–4656. http://dx.doi.org/10.1021/ie030786k.

Lapin, A., Schmid, J., Reuss, M., 2006. Modeling the dynamics of e. Coli populations in the three-dimensional turbulent field of a stirred-tank bioreactor—A structured–segregated approach. Chem. Eng. Sci. 61 (14), 4783–4797. http://dx.doi.org/10.1016/j.ces.2006.03.003.

Lara, A.R., Galindo, E., Ramírez, O.T., Palomares, L.A., 2006. Living with heterogeneities in bioreactors: understanding the effects of environmental gradients on cells. Mol. Biotechnol. 34 (3), 355–382. http://dx.doi.org/10.1385/MB:34:3:355.

Larsson, G., Törnkvist, M., Wernersson, E.S., Trägårdh, C., Noorman, H., Enfors, S.O., 1996. Substrate gradients in bioreactors: Origin and consequences. Bioprocess Eng. 14 (6), 281–289. http://dx.doi.org/10.1007/BF00369471.

Lauterbach, T., Lüke, T., Büker, M.-J., Hedayat, C., Gernandt, T., Moll, R., Grösel, M., Lenk, S., Seidel, F., Brunner, D., Bley, T., Walther, T., Lenk, F., 2019. Measurements on the fly– introducing mobile micro-sensors for Biotechnological applications. Sensors Actuators A 287, 29–38. http://dx.doi.org/10.1016/j.sna.2019.01.003.

Mann, R., Mavros, P., Middleton, J.C., 1981. A structured stochastic flow model for interpreting flow-follower data from a stirred vessel. Trans. Inst. Chem. Eng. 59 (4), 271–278.

Meier, S.J., 2005. Cell culture scale-up: Mixing, mass transfer, and use of appropriate scale-down models. In: Biochemical Engineering XIV. vol. XIV, Harrison Hot Springs, Canada.

Middleton, J.C., 1979. Measurement of circulation within large mixing vessels. In: Proceedings of the 3rd European Conference on Mixing: Held At the University of York, vol. 1, BHRA Fluid Engineering, Cranfield, Bedford, England, pp. 15–36.

Mitchell, F.R.G., 1969. Low power telemetry for circulation studies. J. Phys. E: Sci. Instrum. 2 (9), 812. http://dx.doi.org/10.1088/0022-3735/2/9/416.

Mittermeier, F., Bäumler, M., Arulrajah, P., García Lima, J.d., Hauke, S., Stock, A., Weuster-Botz, D., 2022. Artificial microbial consortia for bioproduction processes. Eng. Life Sci. 23 (1), e2100152. http://dx.doi.org/10.1002/elsc.202100152.

Nadal-Rey, G., McClure, D.D., Kavanagh, J.M., Cassells, B., Cornelissen, S., Fletcher, D.F., Gernaey, K.V., 2021a. Development of dynamic compartment models for industrial aerobic fed-batch fermentation processes. Chem. Eng. J. 420, 130402. http://dx.doi.org/10.1016/j.cej.2021.130402.

Nadal-Rey, G., McClure, D.D., Kavanagh, J.M., Cornelissen, S., Fletcher, D.F., Gernaey, K.V., 2021b. Understanding gradients in industrial bioreactors. Biotechnol. Adv. 46, 107660. http://dx.doi.org/10.1016/j.biotechadv.2020.107660.

Neubauer, P., Junne, S., 2010. Scale-down simulators for metabolic analysis of large-scale bioprocesses. Curr. Opin. Biotechnol. 21 (1), 114–121. http://dx.doi.org/10.1016/j.copbio.2010.02.001.

Neubauer, P., Junne, S., 2016. Scale-up and scale-down methodologies for bioreactors. In: Bioreactors. John Wiley & Sons, Ltd, pp. 323–354. http://dx.doi.org/10.1002/9783527683369.ch11.

Nienow, A.W., 1996. On impeller circulation and mixing effectiveness in the turbulent flow regime. Chem. Eng. Sci. 52 (15), 2557–2565. http://dx.doi.org/10.1016/S0009-2509(97)00072-9.

Nienow, A.W., 1998. Hydrodynamics of stirred bioreactors. Appl. Mech. Rev. 51 (1), 3–32. http://dx.doi.org/10.1115/1.3098990.

Nienow, A.W., 2006. Reactor engineering in large scale animal cell culture. Cytotechnology 50 (1–3), 9–33. http://dx.doi.org/10.1007/s10616-006-9005-8.

Nienow, A.W., 2014. Re "development of a scale-down model of hydrodynamic stress to study the performance of an industrial CHO cell line under simulated production scale bioreactor conditions" [Sieck, J.B., Cordes, T., Budach, W.E., Rhiel, M.H., Suemeghy, Z., Leist, C., Villiger, T.K., Morbidelli, M., Soos, M., 2013. Journal of Biotechnology 164, 41–49]. J. Biotechnol. 171, 82–84. http://dx.doi.org/10.1016/j.jbiotec.2013.12.002.

Nienow, A.W., 2021. The impact of fluid dynamic stress in stirred bioreactors – the scale of the biological entity: A personal view. Chem. Ing. Tech. 93 (1–2), 17–30. http://dx.doi.org/10.1002/cite.202000176.

Nienow, A.W., Isailovic, B., Barrett, T.A., 2016. Design and performance of single-use, stirred-tank bioreactors. Bioprocess Int. 14 (10), 12–21.

Nienow, A.W., Scott, W.H., Hewitt, C.J., Thomas, C.R., Lewis, G., Amanullah, A., Kiss, R., Meier, S.J., 2013. Scale-down studies for assessing the impact of different stress parameters on growth and product quality during animal cell culture. Chem. Eng. Res. Des. 91 (11), 2265–2274. http://dx.doi.org/10.1016/j.cherd.2013.04.002.

Noorman, H., 2011. An industrial perspective on bioreactor scale-down: what we can learn from combined large-scale bioprocess and model fluid studies. Biotechnol. J. 6 (8), 934–943. http://dx.doi.org/10.1002/biot.201000406.

O'Neill, K., Larsen, J., Curtis, W., 2008. Scale-up of agrobacterium-mediated transient protein expression in bioreactor-grown nicotiana glutinosa plant cell suspension culture. Biotechnol. Prog. 24 (2), 372–376. http://dx.doi.org/10.1021/bp0703127.

Ouellette, N.T., O'Malley, P.J.J., Gollub, J.P., 2008. Transport of finite-sized particles in chaotic flow. Phys. Rev. Lett. 101 (17), 174504. http://dx.doi.org/10.1103/PhysRevLett.101.174504.

Paul, E.L., Atiemo-Obeng, V.A., Kresta, S.M. (Eds.), 2004. Handbook of Industrial Mixing: Science and Practice. Wiley-Interscience, Hoboken, NJ, USA.

Petry, F., Salzig, D., 2022. Large-scale production of size-adjusted β-cell spheroids in a fully controlled stirred-tank reactor. Processes 10 (5), 861. http://dx.doi.org/10.3390/pr10050861.

Qian, Y., Xing, Z., Lee, S., Mackin, N.A., He, A., Kayne, P.S., He, Q., Qian, N.-X., Li, Z.J., 2014. Hypoxia influences protein transport and epigenetic repression of CHO cell cultures in shake flasks. Biotechnol. J. 9 (11), 1413–1424. http://dx.doi.org/10.1002/biot.201400315.

Reinecke, S.F., 2013. Instrumentierte Strömungsfolger zur Prozessdiagnose in gerührten Fermentern (Ph.D. thesis). Dresden University of Technology, Dresden.

Reinecke, S.F., Buntkiel, L., Kipping, R., Hampel, U., 2022. Process characterization in industrial vessels by flow-following sensor particles. Meas. Sci. Technol. 33 (9), 095106. http://dx.doi.org/10.1088/1361-6501/ac75af.

Reinecke, S., Deutschmann, A., Jobst, K., Kryk, H., Friedrich, E., Hampel, U., 2012. Flow following sensor particles—validation and macro-mixing analysis in a stirred fermentation vessel with a highly viscous substrate. Biochem. Eng. J. 69, 159–171. http://dx.doi.org/10.1016/j.bej.2012.09.010.

Rosseburg, A., Fitschen, J., Wutz, J., Wucherpfennig, T., Schlüter, M., 2018. Hydrodynamic inhomogeneities in large scale stirred tanks – influence on mixing time. Chem. Eng. Sci. 188, 208–220. http://dx.doi.org/10.1016/j.ces.2018.05.008.

Rotondi, M., Grace, N., Betts, J., Bargh, N., Costariol, E., Zoro, B., Hewitt, C.J., Nienow, A.W., Rafiq, Q.A., 2021. Design and development of a new ambr250® bioreactor vessel for improved cell and gene therapy applications. Biotechnol. Lett. 43 (5), 1103–1116. http://dx.doi.org/10.1007/s10529-021-03076-3.

Rugbjerg, P., Sommer, M.O.A., 2019. Overcoming genetic heterogeneity in industrial fermentations. Nature Biotechnol. 37 (8), 869–876. http://dx.doi.org/10.1038/s41587-019-0171-6.

Schubert, H., 2008. Handbuch der mechanischen Verfahrenstechnik: Partikeleigenschaften, Mikroprozesse, Makroprozesse, Zerteilen, Agglomerieren, Trennen, Mischen, Schüttgut, 1. Aufl., 1. Nachdr Wiley-VCH, Weinheim.

Siebler, F., Lapin, A., Hermann, M., Takors, R., 2019. The impact of CO gradients on C. Ljungdahlii in a 125 M3 bubble column: mass transfer, circulation time and lifeline analysis. Chem. Eng. Sci. 207, 410–423. http://dx.doi.org/10.1016/j.ces.2019.06.018.

Sieblist, C., Jenzsch, M., Pohlscheidt, M., Lübbert, A., 2011. Insights into large-scale cell-culture reactors: I. liquid mixing and oxygen supply. Biotechnol. J. 6 (12), 1532–1546. http://dx.doi.org/10.1002/biot.201000408.

Sieck, J.B., Cordes, T., Budach, W.E., Rhiel, M.H., Suemeghy, Z., Leist, C., Villiger, T.K., Morbidelli, M., Soos, M., 2013. Development of a scale-down model of hydrodynamic stress to study the performance of an industrial CHO cell line under simulated production scale bioreactor conditions. J. Biotechnol. 164 (1), 41–49. http://dx.doi.org/10.1016/j.jbiotec.2012.11.012.

Simmons, M., Zhu, H., Bujalski, W., Hewitt, C., Nienow, A., 2007. Mixing in a model bioreactor using agitators with a high solidity ratio and deep blades. Chem. Eng. Res. Des. 85 (5), 551–559. http://dx.doi.org/10.1205/cherd06157.

Ståhl Wernersson, E., Trägårdh, C., 1999. Scale-up of Rushton turbine-agitated tanks. Chem. Eng. Sci. 54 (19), 4245–4256. http://dx.doi.org/10.1016/S0009-2509(99)00127-X.

Stine, J.M., Beardslee, L.A., Chu, S., Liu, S., Motabar, D., Bentley, W.E., Ghodssi, R., 2020a. Wireless sensor-integrated platform for localized dissolved oxygen sensing in bioreactors. J. Microelectromech. Syst. 29 (5), 713–719. http://dx.doi.org/10.1109/JMEMS.2020.2999089.

Stine, J.M., Beardslee, L.A., Sathyam, R.M., Bentley, W.E., Ghodssi, R., 2020b. Electrochemical dissolved oxygen sensor-integrated platform for wireless in situ bioprocess monitoring. Sensors Actuators B 320, 128381. http://dx.doi.org/10.1016/j.snb.2020.128381.

Takors, R., 2012. Scale-up of microbial processes: impacts, tools and open questions. J. Biotechnol. 160 (1–2), 3–9. http://dx.doi.org/10.1016/j.jbiotec.2011.12.010.

Tatterson, G.B., 1991. Fluid Mixing and Gas Dispersion in Agitated Tanks. McGraw-Hill Companies, New York.

Todtenberg, N., Schmitz-Hertzberg, S.-T., Schmalz, K., Klatt, J., Jorde, F., Juttner, B., Kraemer, R., 2015. Autonomous sensor capsule for usage in bioreactors. IEEE Sens. J. 15 (7), 4093–4102. http://dx.doi.org/10.1109/JSEN.2015.2412652.

Tropea, C., Yarin, A.L., Foss, J.F. (Eds.), 2007. Springer handbook of experimental fluid mechanics. Springer, Berlin.

Van Barneveld, J., Smit, W., Oosterhuis, N.M.G., Pragt, H.J., 1987a. Measuring the liquid circulation time in a large gas-liquid contactor by means of a radio pill. part 1. flow pattern and mean circulation time. Ind. Eng. Chem. Res. 26 (11), 2185–2192. http://dx.doi.org/10.1021/ie00071a003.

Van Barneveld, J., Smit, W., Oosterhuis, N.M.G., Pragt, H.J., 1987b. Measuring the liquid circulation time in a large gas-liquid contactor by means of a radio pill. Part 2. circulation time distribution. Ind. Eng. Chem. Res. 26 (11), 2192–2195. http://dx.doi.org/10.1021/ie00071a004.

van de Vusse, J.G., 1962. A new model for the stirred tank reactor. Chem. Eng. Sci. 17 (7), 507–521. http://dx.doi.org/10.1016/0009-2509(62)87002-X.

Vasconcelos, J.M., Alves, S., Barata, J.M., 1995. Mixing in gas-liquid contactors agitated by multiple turbines. Chem. Eng. Sci. 50 (14), 2343–2354. http://dx.doi.org/10.1016/0009-2509(95)00090-R.

Voncken, R., Holmes, D., Den Hartog, H., 1964. Fluid flow in turbine-stirred, baffled tanks—II. Chem. Eng. Sci. 19 (3), 209–213. http://dx.doi.org/10.1016/0009-2509(64)85031-4.

Vrábel, P., van der Lans, R.G., Cui, Y., Luyben, K.C., 1999. Compartment model approach: mixing in large scale aerated reactors with multiple impellers. Chem. Eng. Res. Des. 77 (4), 291–302. http://dx.doi.org/10.1205/026387699526223.

Vrábel, P., van der Lans, R.G., Luyben, K.C., Boon, L., Nienow, A.W., 2000. Mixing in large-scale vessels stirred with multiple radial or radial and axial up-pumping impellers: Modelling and measurements. Chem. Eng. Sci. 55 (23), 5881–5896. http://dx.doi.org/10.1016/S0009-2509(00)00175-5.

Wang, G., Wang, X., Yang, Q., Haringa, C., Wang, Z., Chu, J., Zhuang, Y.-P., 2023. An Industrial Perspective on in Vivo Kinetics of Central Metabolite Pools and Dynamic Flux Responses in Penicillium Chrysogenum during Periodic Dissolved Oxygen Feast-Famine Cycles in a Scale-down System. Preprint, Preprints, http://dx.doi.org/10.22541/au.169117945.56080335/v1.

Weetman, R.J., Oldshue, J.Y., 1988. Power, flow and shear characteristics of mixing impellers. In: Proceedings of the 6th European Conference on Mixing, Pavia, Italy (1988), vol. 6, AIDIC/BHR Group, Cranfield, UK, Pavia, Italy, pp. 43–50.

Weiland, C., Steuwe, E., Fitschen, J., Hoffmann, M., Schlüter, M., Padberg-Gehle, K., von Kameke, A., 2023. Computational study of three-dimensional Lagrangian transport and mixing in a stirred tank reactor. Chem. Eng. J. Adv. 14, 100448. http://dx.doi.org/10.1016/j.ceja.2023.100448.

Wurm, F.M., 2004. Production of recombinant protein therapeutics in cultivated mammalian cells. Nature Biotechnol. 22 (11), 1393–1398. http://dx.doi.org/10.1038/nbt1026.

Zhu, H., Nienow, A.W., Bujalski, W., Simmons, M.J., 2009. Mixing studies in a model aerated bioreactor equipped with an up- or a down-pumping 'elephant ear' agitator: power, hold-up and aerated flow field measurements. Chem. Eng. Res. Des. 87 (3), 307–317. http://dx.doi.org/10.1016/j.cherd.2008.08.013.

Zlokarnik, M., 1967. Eignung von Rührern Zum Homogenisieren von Flüssigkeitsgemischen. Chem. Ing. Tech. 39 (9), 539–548.

Zlokarnik, M., 2001. Stirring: Theory and Practice. Wiley-VCH Verlag GmbH, Weinheim, Germany.